Received: 7 May 2024 | Revised: 28 August 2024 | Accepted: 12 September 2024

DOI: 10.1111/sapm.12767

STUDIES IN APPLIED MATHEMATICS WILEY

ORIGINAL ARTICLE

Hydrodynamics of a discrete conservation law

Patrick Sprenger[1] | **Christopher Chong**[2] | **Emmanuel Okyere**[2] | **Michael Herrmann**[3] | **P. G. Kevrekidis**[4] | **Mark A. Hoefer**[5]

[1]Department of Applied Mathematics, University of California Merced, Merced, California, USA

[2]Department of Mathematics, Bowdoin College, Brunswick, Maine, USA

[3]Institute of Partial Differential Equations, Technische Universität Braunschweig, Braunschweig, Germany

[4]Department of Mathematics and Statistics, University of Massachusetts Amherst, Amherst, Massachusetts, USA

[5]Department of Applied Mathematics, University of Colorado, Boulder, Colorado, USA

Correspondence
Patrick Sprenger, Department of Applied Mathematics, University of California Merced, Merced, CA 95343, USA.
Email: sprenger@ucmerced.edu

Funding information
Isaac Newton Institute for Mathematical Sciences, Grant/Award Number: EP/R014604/1; Simons Foundation, Grant/Award Number: 316017; National Science Foundation, Grant/Award Numbers: DMS-2107945, DMS-2204702, PHY-2110030, DMS-2306319

Abstract

The Riemann problem for the discrete conservation law $2\dot{u}_n + u_{n+1}^2 - u_{n-1}^2 = 0$ is classified using Whitham modulation theory, a quasi-continuum approximation, and numerical simulations. A surprisingly elaborate set of solutions to this simple discrete regularization of the inviscid Burgers' equation is obtained. In addition to discrete analogs of well-known dispersive hydrodynamic solutions—rarefaction waves (RWs) and dispersive shock waves (DSWs)—additional unsteady solution families and finite-time blowup are observed. Two solution types exhibit no known conservative continuum correlates: (i) a counterpropagating DSW and RW solution separated by a symmetric, stationary shock and (ii) an unsteady shock emitting two counterpropagating periodic wavetrains with the same frequency connected to a partial DSW or an RW. Another class of solutions called traveling DSWs, (iii), consists of a partial DSW connected to a traveling wave comprised of a periodic wavetrain with a rapid transition to a constant. Portions of solutions (ii) and (iii) are interpreted as shock solutions of the Whitham modulation equations.

KEYWORDS
dispersive shock waves, Whitham modulation theory, Riemann problem

1 | INTRODUCTION

The hydrodynamics of the conservation law (inviscid Burgers' equation)

$$u_t + \left(u^2\right)_x = 0, \tag{1}$$

with $u(x,t) \in \mathbb{R}$, $x,t \in \mathbb{R}$ is succinctly expressed by solutions of the Riemann problem that consists of Equation (1) for $t > 0$ subject to the initial condition

$$u(x,0) = \begin{cases} u_- & x \le 0, \\ u_+ & x > 0, \end{cases} \quad x \in \mathbb{R} \tag{2}$$

for $u_\pm \in \mathbb{R}$. Solutions must be interpreted in a weak sense and depend intimately upon the regularization applied. For the *viscous regularization* in which Equation (1) is modified to Burgers' equation $u_t + (u^2)_x = \nu u_{xx}$ where $\nu > 0$, the weak solution of (1)—either a moving discontinuity (shock) or rarefaction wave (RW)—is uniquely determined by considering the strong vanishing viscosity limit $\nu \to 0^+$ of Burgers' equation.[1] This results in the well-known Rankine–Hugoniot jump condition for the speed $V = (u_- + u_+)$ and Lax entropy condition $u_+ < V < u_-$ of admissible shock solutions. Regularization by more complex viscous terms (nonlinear, higher order, and viscous-dispersive) generally results in the same weak solution.[2] An alternative *dispersive regularization* is the Korteweg–de Vries (KdV) equation $u_t + (u^2)_x + \varepsilon^2 u_{xxx} = 0$. In this case, the zero dispersion limit $\varepsilon \to 0$ converges weakly in the sense that it satisfies the KdV–Whitham modulation equations corresponding to averaged conservation laws.[1,3] Gurevich and Pitaevskii recognized the physical importance of the asymptotic approximation obtained by considering small but nonzero ε and obtained the dispersive shock wave (DSW) solution of the KdV equation for (2) when $u_- > u_+$ as a self-similar solution of the KdV–Whitham modulation equations.[1,4] They also observed that when $u_- < u_+$, the KdV equation with small but nonzero ε is well-approximated by the same RW obtained from the dispersionless Hopf equation (1). DSWs are unsteady, modulated nonlinear wavetrains connecting two distinct levels.[5] In contrast to viscous regularization, alternative dispersive regularizations can result in drastically different Riemann problem solution behavior in the small dispersion regime, particularly when higher-order[6] or nonlocal[7] dispersive terms are considered. The multiscale dynamics of conservative nonlinear wave equations in the small dispersion regime are generally referred to as dispersive hydrodynamics.[5]

In this paper, we study the dispersive hydrodynamics of the *discrete regularization* of Equation (1)

$$\frac{d}{dt}u_n + \frac{1}{2}\left(u_{n+1}^2 - u_{n-1}^2\right) = 0, \tag{3}$$

by solving the Riemann problem

$$u_n(0) = \begin{cases} u_-, & n \le 0 \\ u_+, & n > 0 \end{cases} \tag{4}$$

for (3) where $n \in \mathbb{Z}, t \in \mathbb{R}, u = u_n(t) \in \mathbb{R}$. Equation (3) is the simplest centered differencing scheme for the hydrodynamic flux. As recognized in the early days of computational fluid dynamics by von Neumann, and later clarified by Lax, differencing schemes like (3) introduce oscillations

that require mitigation if one wishes to converge strongly to viscously regularized solutions that satisfy the conservation laws of fluid dynamics.[8] In this paper, we consider Equation (3), subject to (4), in its own right, divorced from the aim of approximating solutions of Equation (1). The semidiscrete equation (3) can be interpreted as the dispersive regularization

$$u_T + \frac{i}{\varepsilon}\sin(-i\varepsilon\partial_X)\left(u^2\right) = 0 \tag{5}$$

by introducing $T = \varepsilon t$, $X = \varepsilon n$ into Equation (3), where $\varepsilon > 0$ is the lattice spacing. Here, $i\sin(-i\partial_x) = \frac{1}{2}(\exp(\partial_x) - \exp(-\partial_x))$ is the pseudo-differential operator for the centered discrete derivative and acts on a function f in the variable x via

$$(i\sin(-i\partial_x)f)(x) = \frac{1}{2}(f(x+1) - f(x-1)). \tag{6}$$

Equation (5) is similar to Whitham-type evolutionary equations[9–11] except that it is further constrained to be band-limited. For the lattice equation (3) at time t, the support of the discrete-space Fourier transform of $u_n(t)$ is $[-\pi, \pi]$ due to the smallest length scale set by the lattice spacing, whereas the Fourier transform of quasi-continuum approximations is not generally compactly supported. As we will demonstrate, this fundamental property of lattice equations introduces new hydrodynamic solution features that do not appear within certain continuum limits of the model.

Equation (5) can be used to formally derive quasi-continuum approximations by using Padé approximants of $\frac{i}{\varepsilon}\sin(-i\varepsilon\partial_X)$ for $0 < \varepsilon \ll 1$. For example, the (1,3) Padé approximant

$$\frac{i}{\varepsilon}\sin(-i\varepsilon\partial_X) \approx \left(1 - \frac{\varepsilon^2}{6}\partial_X^2\right)^{-1}\partial_X \tag{7}$$

leads to the Benjamin–Bona–Mahoney (BBM) equation absent the linear convective term[12]

$$U_T + (U^2)_X - \frac{\varepsilon^2}{6}U_{XXT} = 0. \tag{8}$$

This quasi-continuum approximation, inspired by the work of Rosenau on mass-spring chains[13,14]—see also the discussion in Ref. 15—is expected to faithfully represent the long-wavelength behavior of the lattice model (3). But it is no longer band-limited. In fact, outside of RWs and DSWs, the Riemann problem solutions we obtain for the lattice equation (3) bear no resemblance to the corresponding Riemann problem solutions of (8) obtained in Ref. 7 where short wave effects become important. Nevertheless, the quasi-continuum model (8) admits exact solitary and periodic traveling wave solutions that can be used to approximate corresponding solutions of the lattice model (3).

A particular feature of the band-limited lattice equation (3), and others with centered differences, is the existence of stationary, period two (binary) oscillation solutions

$$u_{2n} = \alpha, \quad u_{2n+1} = \beta, \quad n \in \mathbb{Z} \tag{9}$$

for any $\alpha, \beta \in \mathbb{R}$. Equation (3) was studied in Ref. 16 using extensive numerical simulations for certain types of odd initial data and binary oscillations were found to play an important role. Allowing for slow spatiotemporal modulations of this solution—$\alpha = \alpha(X,T), \beta = \beta(X,T), T = \varepsilon t$,

$X = \varepsilon n$, $0 < \varepsilon \ll 1$—Turner and Rosales[16] obtained the modulation equations

$$\alpha_T + (\beta^2)_X = 0, \quad \beta_T + (\alpha^2)_X = 0. \tag{10}$$

Two important implications of the hydrodynamic-type equations (10) are: (i) the equations (10) are elliptic whenever $\alpha\beta < 0$ and (ii) the existence of discontinuous, shock solutions satisfying Rankine–Hugoniot jump conditions. The ellipticity of (10) was shown to provide a route through modulated binary oscillations to blowup of solutions of (3).

While the topic of DSWs and dispersive hydrodynamics has been more extensively explored in the realm of continuum media,[5,17] as already implied by the above discussion, studies of the discrete realm have the potential to offer new and intriguing wave features. In addition, the motivation for such explorations has significantly increased on account of a diverse range of corresponding applications. A central topic is the study of granular crystals and associated nonlinear metamaterials,[15] consisting typically of elastically interacting bead chains. There, a sequence of experimental efforts in simpler,[18,19] as well as in progressively more complex media, including dimers[20] and the more recent setup of hollow elliptic cylinders[21] have manifested the spontaneous emergence of DSWs under suitable loading conditions. However, this has not been the only setting where "effectively discrete" DSWs have experimentally emerged. Another example is in nonlinear optics where such structures have appeared in optical waveguide arrays.[22] Finally, and quite recently, yet another setup has emerged, that of tunable magnetic lattices[23] in which ultraslow shock waves can arise and be experimentally imaged.

Earlier interest in lattice shocks include the heyday of conservation laws and shock waves in the 1950s and 1960s when material scientists were interested in the compression of a solid by passage of a very strong shock wave through materials.[24] Early numerical studies (molecular dynamics simulations) depicted what we now call a lattice DSW in the material's stress profile and recognized its unsteady character in a one-dimensional anharmonic chain.[25] This contradicted the basic assumption of steadiness underlying the Rankine–Hugoniot jump conditions and led to some controversy in the field. The DSW's leading edge was then identified with a homoclinic traveling wave solution (solitary wave) of a continuum approximation in Ref. 26, later identified as a generic feature of DSWs in continuum media.[4,27] The controversy continued for about 15 years until, in 1979, three-dimensional lattice simulations were shown to exhibit a transition from unsteady to steady shock fronts due to transverse strains.[28] It is worth noting that the same transition from one-dimensional, unsteady (dispersive) to multidimensional, steady (effectively viscous) shock propagation, was recently observed in a completely different, ultracold atomic superfluid.[29]

These works have motivated the present authors to revisit "lattice hydrodynamics" and the prototypical settings where DSW structures can arise in nonlinear dynamical lattices. Canonical examples of first order in time, quadratically nonlinear lattice nonlinear ordinary differential equations (ODEs) in a conservation law form were discussed extensively in the work of Turner and Rosales.[16] A subset of the present authors has recently revisited this class of models in Ref. 30 attempting to incorporate tools from Whitham modulation theory, bringing to bear both data-driven, as well as more theoretically inspired quasi-continuum approaches to obtain an effective dimensional reduction, through a local ODE description of the unsteady DSW states. Our aim here is to expand on this work, offering a more systematic classification of the possible solutions of such models by using Whitham modulation theory and, where appropriate, quasi-continuum approximation considerations supplemented by direct numerical simulations.

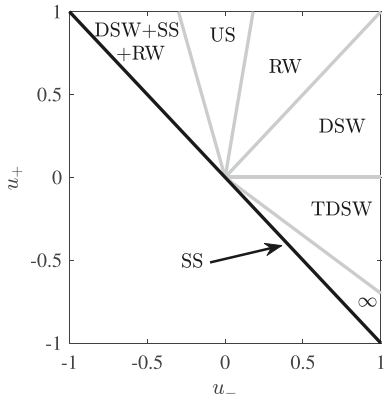

SS	Stationary shock
RW	Rarefaction wave
DSW	Dispersive shock wave
DSW+SS+RW	DSW + stationary shock + RW
TDSW	traveling DSW
∞	Blow up
US	Unsteady shock

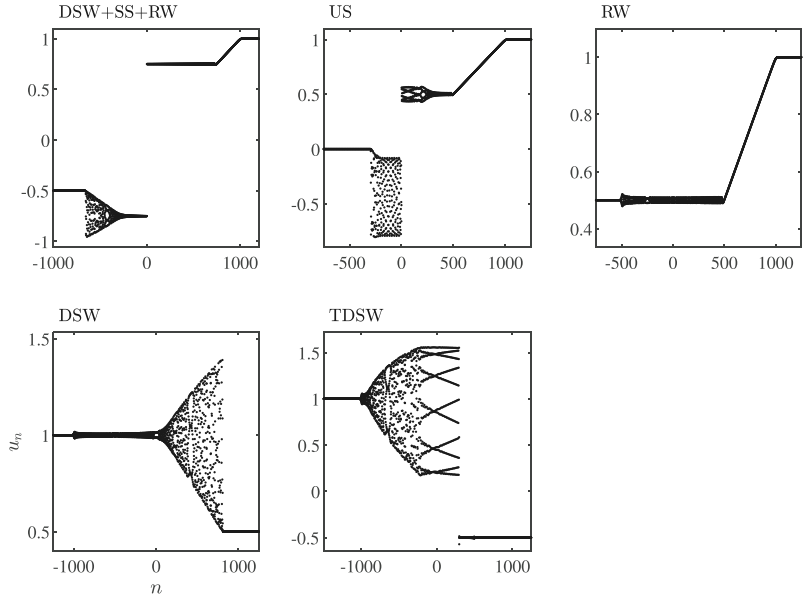

FIGURE 1 Classification of the Riemann problem (4) of the discrete conservation law (3). The numerical computations are shown at $t = 500$ and have been performed with the initial data in (11).

We select the scale-invariant, representative nonlinear example (3) within the class of models of Ref. 16 and set up the corresponding discrete Riemann problem (4). Our motivation for this choice is to contrast the complex and rich nonlinear behavior that the latter model will be seen to feature below with the far simpler dynamical phenomenology of the integrable discretization of Section IIA and of the work of Lax.[31] Figure 1 depicts our phase diagram as a partitioning of the parameter space (u_-, u_+) and identifies seven distinct solution behaviors. Some of these, such as the possibility of an RW or a DSW as well as that of blowup are to a certain degree expected or have been argued to be present previously.[16] They are labeled RW, DSW, and ∞ in Figure 1, respectively. However, there are choices of initial conditions that yield less common dynamical outputs, some of which are genuinely discrete in nature with labels in Figure 1 identified parenthetically. These include, for instance, a stationary, symmetric shock on its own (SS) or separating an RW and a DSW (DSW + SS + RW). Another example is a traveling DSW (TDSW), which consists of a partial DSW connected to a heteroclinic periodic-to-equilibrium traveling wave. Arguably, the most

complex structure encountered is an unsteady shock (US) evolving between two distinct traveling waves featuring the same temporal frequency. In what follows, we explain our partitioning of the phase diagram of Figure 1 into the regions pertaining to these different dynamical behaviors and we offer a set of tools that can be used to understand each one, as well as unveil some open directions for future exploration.

There exists a family of Riemann problems that can be considered in the discrete setting by modifying the value $u_0(0)$ in (4). For example, Turner and Rosales set $u_0(0) = 0$ and $u_- = -u_+$.[16] We primarily focus on the data (4) in which $u_0(0) = u_-$ resulting in the phase diagram of Figure 1. While changing $u_0(0)$ does not affect the observed solution phases, it does change the phase boundaries. We interpret this microscopic modification of the initial data impacting the macroscopic properties of solutions as an indication of nonuniqueness of the Riemann problem for the dispersive regularization (7).

It is important to distinguish our use of the term "shock" or "shock wave" from the classical notion of discontinuous weak solutions of inviscid Burgers' equation (1). We identify four classes of shock solutions to the discrete equation (3) by prefacing each with a descriptor in Figure 1. The simplest is the symmetric, *stationary* shock (SS) solution of the lattice

$$u_n(t) = \begin{cases} -u_0 & n \leq 0, \\ u_0 & n > 0, \end{cases} \tag{11}$$

where $u_0 > 0$. The other shock solutions can be understood as special solutions of the first-order, quasi-linear Whitham modulation equations corresponding to Equation (3) that are described in Section 3. The unsteady DSW is approximated by a nonlinear, periodic wavetrain modulated by an RW solution of the Whitham modulation equations. Note that the DSW does not satisfy the Rankine–Hugoniot jump conditions of the Whitham modulation equations. On the other hand, the US is approximated by two periodic traveling waves that satisfy the jump conditions for the Whitham modulation equations. The TDSW consists of both an unsteady partial DSW—approximated by a rarefaction solution of the Whitham modulation equations—and a steady traveling wave—approximated by a periodic traveling wave and a solitary wave that satisfy the jump conditions for the Whitham modulation equations. There is an important distinction between the traveling wave and US as discontinuous solutions of the Whitham modulation equations. The phase speeds of the two periodic traveling waves in the US solution differ from one another and from the shock speed, which is zero. On the other hand, the traveling wave solution consists of a single periodic traveling wave whose phase speed is the same as the shock speed. For clarity, we summarize the four distinct uses of the term "shock" in this paper:

1. The stationary lattice shock (SS) (11);
2. The unsteady DSW that is approximated by a rarefaction solution of the Whitham modulation equations;
3. The unsteady shock (US) that is approximated by a discontinuous shock solution of the Whitham modulation equations;
4. The traveling dispersive shock wave (TDSW) that is approximated by a shock-rarefaction solution of the Whitham modulation equations.

Our presentation will be structured as follows. In Section 2, we present the model equations, as well as the principal setup and notation for our study. In Section 3, we focus on the Whitham modulation equation formulation for the discrete problem. We discuss the corresponding

conservation laws and how their averaging can provide information for the DSW features of our model. Section 4 is dedicated to the systematic classification of our solutions in the different parametric regimes, accompanied by illustrative numerical computations of the different identified waveforms. In Section 5, we show how modification of the Riemann data (4) at a single site can lead to drastically different solution behaviors. Finally, in Section 6, we summarize our findings and present our conclusions, as well as a number of open questions for further research into this budding theme.

2 | MODEL EQUATIONS

It will be beneficial to generalize Equation (3) and consider the discrete scalar conservation law[16]

$$2\frac{du_n}{dt} + \Phi'(u_{n+1}) - \Phi'(u_{n-1}) = 0, \tag{12}$$

a discretization of the more general conservation law $u_t + \Phi'(u)_x = 0$, where $n \in \mathbb{Z}, t \in \mathbb{R}, u = u_n(t) \in \mathbb{R}$ and the potential $\Phi(u)$ is assumed to be smooth with $\Phi'(u)$ a convex function of its argument $\Phi'''(u) \neq 0$. Equation (12) possesses a Lagrangian and Hamiltonian structure,[32] yet it is first order only, making its analysis slightly more convenient when compared to classical nonlinear oscillators, such as those of the Fermi–Pasta–Ulam–Tsingou (FPUT) type.[33] Besides serving as a prototype model for lattice DSWs, Equation (12) is also of interest for applications, such as in the description of traffic flow[34]; for a discussion of relevant models and their continuum limits see also Ref. 16.

In this paper, we primarily focus on the potential

$$\Phi(u) = \frac{u^3}{3}. \tag{13}$$

For this choice, Turner and Rosales[16] showed that two quantities are conserved across the lattice. The "mass"

$$M(t) = \sum_n u_n(t)$$

and "energy"

$$E(t) = \sum_n \Phi(u_n(t)),$$

when well-defined, are conserved in the infinite lattice and in a finite lattice with periodic boundary conditions. It is not known to the authors if other conservation laws are available for Equation (3), but the nonintegrability of the system suggests that more conservation laws are unlikely. The linear dispersion relation for Equation (12) is

$$\omega_0(k, \bar{u}) = \Phi''(\bar{u})\sin(k), \quad k, \bar{u} \in \mathbb{R} \tag{14}$$

for linearized wave solutions of the form $u_n(t) = \bar{u} + ae^{i(kn-\omega_0 t)}$, $|a| \ll 1$. Throughout the manuscript, we consider the Riemann, step initial data (4). For numerical simulations, the infinite lattice is truncated by introducing $N > 0$ (even) to represent the number of lattice sites. The

corresponding spatial domain is $-N/2+1 < n \leq N/2$ and the simulation temporal domain is $[0, T_f/\varepsilon]$, where T_f is a fixed constant independent of $\varepsilon = 1/N$. We use free boundary conditions $u_{-N/2} = u_{-N/2+1}$ and $u_{N/2} = u_{N/2-1}$ in conjunction with the initial data equation (4), and we choose domain sizes large enough that interactions with the boundary are negligible. When investigating finite-time blowup, we employ periodic conditions. This allows us to monitor if the rescaled quantities $E(t) \to E(t)/N$ and $M(t) \to M(t)/N$ are conserved (details in Section 4.6). A variational integrator is used for simulations (see Ref. 32). Simulations were also carried out with a Runge–Kutta method to check for consistency which yielded negligible differences on the timescales considered in this paper (for cases that did not involve blow-up features). Due to the scaling symmetry $t \to at$, $u_n \to au_n$, for any nonzero $a \in \mathbb{R}$ of Equation (12) subject to (13), we can set either $u_+ = 1$ or $u_- = 1$ without loss of generality. Figure 1 shows a classification of the zoology of solutions that arise from the Riemann problem. They include RWs for $u_+ = 1$ and $u_- \in (0.18, 1)$, DSWs for $u_+ \in (0, 1)$ and $u_- = 1$, solutions consisting of DSW + SS + RW for $u_+ = 1$ and $u_- \in (-1, -0.26)$, solutions consisting of TDSWs for $u_+ \in (-0.724, 0)$ and $u_- = 1$, US for $u_+ = 1$ and $u_- \in (-0.26, 0.18)$, and blowup (∞) for $u_+ \in (-1, -0.724)$ and $u_- = 1$. The region boundaries are approximate. In Section 4, we provide a detailed analysis for each of the five solution types just described, starting first with the simplest, and moving through them gradually in terms of their complexity according to the table in Figure 1. We employ a number of tools for the study of these solutions, including direct numerical simulation, fixed-point iteration schemes, modulation theory, weak solutions, DSW fitting, and quasi-continuum modeling. The details of these approaches will be given in the sections they are employed, with the exception of modulation theory. This analysis is slightly more involved, and thus has a dedicated section. Our intention in presenting these tools is to leverage this specific, but interesting in its own right, example in order to utilize a variety of techniques that may be of broader relevance to applications in other Hamiltonian nonlinear dynamical lattices. It would be of particular interest to identify similar phenomena or/and to leverage the techniques utilized herein in other dispersive, nonlinear lattice models.

2.1 | An alternative, integrable discretization

Prior to describing the solutions of Equation (3) depicted in Figure 1, we briefly comment on the alternative discretization

$$\frac{du_n}{dt} + u_n(u_{n+1} - u_{n-1}) = 0, \tag{15}$$

of Equation (1) subject to (13). This equation was studied in Refs. 31, 35 where it was shown to exhibit DSWs and, for positive data, to be completely integrable by a transformation[36] to an equation related to the Toda lattice.[37] We have performed numerical simulations of Equation (15) subject to the Riemann data (4) and observe DSWs when $u_- > u_+ \geq 0$, RWs when $u_+ > u_- \geq 0$, and blowup when u_+ and u_- exhibit opposite signs. Examples of numerical simulations of DSWs and RWs that emerge from strictly positive initial Riemann data are shown in Figure 2.

Of course, complete integrability confers a great deal of mathematical structure. Whitham modulation theory for the Toda lattice was developed in Refs. 38–40 while the inverse scattering transform for the Toda lattice with step-type initial data was developed in Ref. 41; see also the recent discussion of Whitham theory applied to DSWs in the Toda lattice.[42] Collectively, these works support our numerical observation that, for positive Riemann data, Equation (15) exhibits only RW and DSW solutions. These Riemann problem solution behaviors are to be contrasted

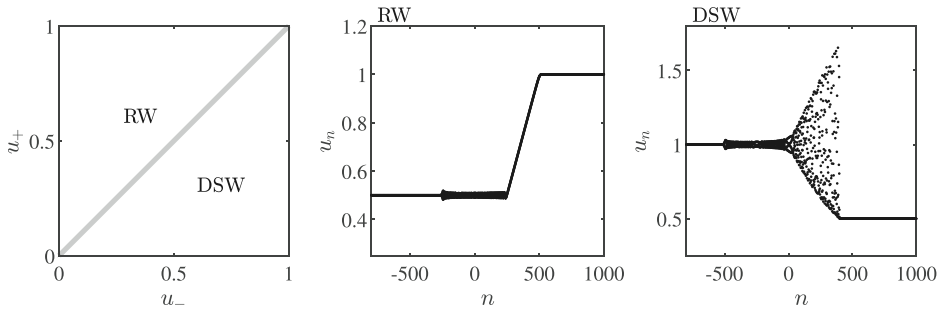

FIGURE 2 Classification of the Riemann problem of (4) (left panel) and typical time evolutions of the Riemann data for a rarefaction wave (RW, middle) and a dispersive shock wave (DSW, right panel) within Equation (15).

with those depicted in Figure 1. Although integrability of Equation (15) is lost for sign-indefinite initial data, the only dynamics we numerically observe are indicative of blowup. Thus, the discretization (3) we focus on in this paper, admits a wider variety of dynamics than the integrable alternative of (15).

3 | WHITHAM THEORY

3.1 | Modulation equations for a continuum system

In this section, we consider a continuum model system by introducing the interpolating function $u(x,t)$ such that $u(n,t) = u_n(t)$ for all $n \in \mathbb{Z}$. This allows us to represent the advance-delay operator in the discrete system (12) as a pseudo-differential operator. The resulting continuum model is

$$u_t + i\sin(-i\partial_x)\left(\Phi'(u)\right) = 0. \tag{16}$$

Equation (16) can be written in the Hamiltonian form

$$u_t = J\frac{\delta H}{\delta u}, \tag{17}$$

where $J = i\sin(-i\partial_x)$ is the antisymmetric operator and $H = \int \Phi(u)\,dx$ is the Hamiltonian. Periodic solutions of (16) are of the form $u(x,t) = \varphi(\theta;\mathbf{q})$ with phase $\theta = kx - \omega t$ and parameters $\mathbf{q} \in \mathbb{R}^3$ (e.g., wavenumber, amplitude, and mean). They satisfy

$$-\omega\varphi_\theta + i\sin(-ik\partial_\theta)\Phi'(\varphi) = 0\,, \tag{18}$$

which is equivalent to the nonlinear advance-delay differential equation

$$2\,\omega\,\varphi_\theta(\theta) = \Phi'(\varphi(\theta+k)) - \Phi'(\varphi(\theta-k)). \tag{19}$$

The solution theory of such nonlocal equations is rather intricate but the existence of a three-parameter family of traveling waves has been established in Ref. 32 by variational techniques.

Integrating (18) once with respect to θ

$$-c_{\mathrm{p}}\varphi + \mathrm{sinc}(-ik\partial_\theta)\Phi'(\varphi) = A, \tag{20}$$

where $c_{\mathrm{p}} = \frac{\omega}{k}$ is the phase speed and A is a real constant. The pseudo-differential operator is then interpreted as a multiplier on the Fourier coefficients of φ,

$$\mathrm{sinc}(-ik\partial_\theta)\Phi'(\varphi) = \sum_n \mathrm{sinc}(nk)\widehat{p}_n \mathrm{e}^{in\theta}, \tag{21}$$

$$\hat{p}_n = \frac{1}{2\pi}\int_0^{2\pi} \Phi'(\varphi(\theta))\mathrm{e}^{-in\theta}d\theta. \tag{22}$$

Equation (16) possesses the two conserved quantities

$$M(t) = \int u dx, \tag{23}$$

$$E(t) = \int \Phi(u) dx, \tag{24}$$

where the domain of integration is determined by the decay or periodicity of u. We now seek the modulation equations for a periodic wave with the slowly varying ansatz

$$u(x,t) = \varphi(\theta;\mathbf{q}(X,T)) + \varepsilon\varphi_1(\theta,X,T) + \cdots, \quad X = \varepsilon x, \quad T = \varepsilon t, \quad 0 < \varepsilon \ll 1, \tag{25}$$

in which the leading-order term $\varphi(\theta;\mathbf{q})$ is the periodic traveling wave solution satisfying (20) with vector of parameters $\mathbf{q}$ that varies on the slow scales X and T while φ is 2π-periodic in θ. We impose the generalized wavenumber and frequency relationships $\theta_x = k$ and $\theta_t = -\omega$ along with their compatibility

$$k_T + \omega_X = 0. \tag{26}$$

Lemma 1. *The nonlocal operator acting on a modulated periodic function $g(\theta,X,T) \in C^1$ has the multiple-scale expansion*

$$\begin{aligned}\sin(-i\partial_x)g &= \sin(-ik\partial_\theta - i\varepsilon\partial_X)g \\ &\sim \sin(-ik\partial_\theta)g - i\frac{\varepsilon}{2}\left(\cos(-ik\partial_\theta)g_X + (\cos(-ik\partial_\theta)g)_X\right) + \mathcal{O}(\varepsilon^2).\end{aligned} \tag{27}$$

Proof. The proof follows from the analyticity of $\sin(\cdot)$. A detailed proof follows all of the ideas in Ref. 11. □

We now average Equation (16) and its higher-order conserved densities by introducing the averaging operator

$$\overline{F[\varphi]}(X,T) = \frac{1}{2\pi}\int_0^{2\pi} F[\varphi(\theta;\mathbf{q}(X,T))]\, d\theta, \tag{28}$$

where $F[u(x,t)] = F(u, u_x, u_t, u_{xt}, ...)$ is a local function of u and its derivatives. If u is a multiscale function of the form $u = g(\theta, X, T)$, then

$$\begin{aligned}\overline{\partial_t F} &= -\omega\overline{\partial_\theta F} + \varepsilon\partial_T\overline{F} = \varepsilon\partial_T\overline{F},\\ \overline{\partial_x F} &= k\overline{\partial_\theta F} + \varepsilon\partial_X\overline{F} = \varepsilon\partial_X\overline{F},\end{aligned} \tag{29}$$

by virtue of the fact that $F = F[g]$ is periodic in θ so the period average of $\partial_\theta F[g]$ is zero. We use Lemma 1 to compute averages of, for example, $\sin(-ik\partial_\theta)g$ for any $g \in L_2([0, 2\pi])$ with the Fourier series $g = \sum_n \hat{g}_n e^{in\theta}$

$$\overline{\sin(-ik\partial_\theta)g} = \overline{\sum_n \sin(nk)\hat{g}_n e^{in\theta}} = 0. \tag{30}$$

We now insert the multiple scales ansatz (25) into the two conservation laws associated with (16), and average. This procedure results in the system of conservation laws

$$\overline{\varphi}_T + \overline{\Phi'(\varphi)}_X = 0, \tag{31a}$$

$$\overline{\Phi(\varphi)}_T + \frac{1}{2}\left(\sum_m \cos(mk)\hat{p}_m^2\right)_X = 0, \tag{31b}$$

$$k_T + \omega_X = 0. \tag{31c}$$

In the vanishing amplitude $a \to 0$ limit, Equations (31a) and (31b) become the Hopf equation

$$\bar{u}_T + \Phi''(\bar{u})\bar{u}_X = 0 \tag{32}$$

for the mean $\bar{u} = \overline{\varphi}$, and the conservation of waves equation (31c) corresponds to linear wave modulation theory with frequency $\omega = \omega_0$ given by the linear dispersion relation (14).

The nonlinear modulation equations can alternatively be derived by employing Whitham's other method of an averaged Lagrangian functional, see for instance, Refs.[1], Chap. 14] and [[43] for symplectic partial differential equations (PDEs),[44–47] for an application to FPUT chains as the most prominent example of Hamiltonian lattices, and Ref. [30] for the discrete conservation law (12). In this setting, the modulation equations take the form

$$\overline{u}_T + (E_{\overline{u}})_X = 0, \tag{33a}$$

$$k_T + (E_S)_X = 0, \tag{33b}$$

$$S_T + (E_k)_X = 0. \tag{33c}$$

This is a system of Hamiltonian PDEs with density variables $\overline{u}$, k, and S, which represent the wave mean, the nonlinear wavenumber, and a nonlocal auxiliary variable that might be regarded as a generalized wave momentum. Moreover, the equation of state $E = E(\overline{u}, k, S)$ describes the energy of a traveling wave and its partial derivatives provide the fluxes in (33). The energy is also

conserved according to the extra conservation law

$$E_T + \left(\frac{1}{2} E_{\overline{u}}^2 + E_k E_S \right)_X = 0 \,, \tag{33d}$$

which is implied by (33) thanks to the chain rule. A closer look to the derivation of (33) in Ref. 30 reveals that (31a) and (31c) correspond to (33a) and (33b), respectively, while (31c) is the analog to (33d). A complete understanding of (31) and (33) is currently out of reach because we are not able to characterize the analytical properties of the constitutive relations since these depend in a very implicit and not tractable way on the three-dimensional solution sets of the nonlinear advance-delay-differential equation (18). For instance, it is not even clear for which values of the parameters, the Whitham system (33) is hyperbolic or genuinely nonlinear. For this reason, we do not work with the full lattice modulation equations directly but combine different approximation procedures with a careful evaluation of numerical data.

3.2 | Relation to the lattice dynamics

Although neither analytical nor numerical solutions to the nonlinear modulation systems (31) or (33) are available, we can extract important partial information from numerical simulations of initial-value problems to (12). The key observation is that the lattice ODE as well as an implied energy equation represent discrete counterparts of local conservation laws and transform under the hyperbolic scaling of space and time into first-order PDEs. To see this, we fix a *window function* χ that depends smoothly on the macroscopic variables (X, T), decays sufficiently fast, and has normalized integral. Using a shifted copy of χ, we are able to quantify the local moments of any microscopic observable near a fixed macroscopic point. For instance, the average

$$\langle u_n \rangle (X, T) = \varepsilon^2 \sum_{\check{n}} \int u_{\check{n}}(\check{t}\,)\, \chi(\varepsilon \check{t} - T, \varepsilon \check{n} - X)\, d\check{t} \,, \qquad T = \varepsilon\, t \,, \qquad X = \varepsilon\, n \tag{34}$$

represents the *mesoscopic space-time averages* of $u_n(t)$ near the macroscopic point (X, T).

Lemma 2. *Any bounded solution to (12) satisfies in the hyperbolic scaling limit $\varepsilon \to 0$ the conservation laws*

$$\partial_T \left\langle u_n \right\rangle + \partial_X \left\langle \Phi'(u_n) \right\rangle = 0, \tag{35a}$$

$$\partial_T \langle \Phi(u_n) \rangle + \partial_X \left\langle \frac{1}{2}\, \Phi'(u_n)\, \Phi'(u_{n+1}) \right\rangle = 0 \tag{35b}$$

provided that these are interpreted in a distributional sense.

Proof. We only give an informal derivation but mention that an alternative and more elegant framework is provided by the theory of Young measures. The latter can also be applied to non-smooth window functions χ and reveals that the mesoscopic averages $\langle \cdot \rangle$ can be expected to be independent of the particular choice for χ. Using the abbreviation $p_n = \Phi'(u_n)$, discrete

integration by parts as well as the smoothness of χ we verify

$$\begin{aligned}\left\langle \frac{1}{2}p_{n+1} - \frac{1}{2}p_{n-1} \right\rangle (X,T) &= \varepsilon^3 \sum_{\check{n}} \int p_{\check{n}}(\check{t}) \left(\frac{1}{2}\chi(\varepsilon\check{t} - T, \varepsilon\check{n} - \varepsilon - X) - \frac{1}{2}\chi(\varepsilon\check{t} - T, \varepsilon\check{n} + \varepsilon - X) \right) d\check{t} \\ &= -\varepsilon^3 \sum_{\check{n}} \int p_{\check{n}}(\check{t}) \partial_X \chi(\varepsilon\check{t} - T, \varepsilon\check{n} - X)\, d\check{t} + \text{h.o.t.} \\ &= -\varepsilon\, \partial_X \left\langle p_n \right\rangle (X,T) + \text{h.o.t.}\end{aligned}$$

and by similar computations we obtain

$$\left\langle \dot{u}_{n+1} \right\rangle (X,T) = -\varepsilon\, \partial_T \left\langle u_n \right\rangle (X,T) + \text{h.o.t.}$$

The asymptotic validity of (35a) is thus a direct consequence of the microscopic dynamics (12), the definition of the bracket $\langle\cdot\rangle$ in (34), and the hyperbolic scaling. The lattice ODE (12) implies with

$$\frac{d}{dt}\Phi(u_n) + \left(\frac{1}{2}\Phi'(u_n)\Phi'(u_{n+1}) \right) - \left(\frac{1}{2}\Phi'(u_{n-1})\Phi'(u_n) \right) = 0\,,$$

another discrete conservation law (in which the time derivative of a density is balanced by the discrete divergence of a flux quantity), so the second claim (35a) can be justified along the same lines. □

There is an important difference between the conservation laws in (31) and (35). The PDEs in (31) (and likewise those in Equation 33) are derived under the *hypothesis* that the lattice solution can be approximated by a modulated traveling wave, see (25), and the closure relations involve the (unknown) profile functions for traveling lattice waves as well as averages with respect to the scalar phase variable θ. Numerical simulations with well-prepared initial data (e.g., the Riemann initial data 4) indicate that the approximation assumption concerning the microscopic data is indeed satisfied but no rigorous proof is available, neither for the lattice (12) nor for FPUT chains with convex interaction potential. The only exceptions are the few completely integrable cases but the details are still complicated and involve special coordinates related to the Lax structure. In particular, even for the lattice of Equation (15) and the Toda chain it is not easy to compute how the phase averages in the modulation equations depend on the traveling wave parameters.

The status of (35) is completely different. The two PDEs can be established under very mild assumptions (boundedness of lattice solutions) and by means of fundamental mathematical principles (such as integration by parts and compactness in the sense of Young measures). They reflect universal constraints for the macroscopic dynamics, do not require any a priori knowledge on the fine structure of the microscopic oscillations, and hold for a large class of initial data (which might even be oscillatory or random). Moreover, the mesoscopic space-time averages can easily by extracted from numerical data. In the simplest case, we use a straightforward box counting with space-time windows of microscopic length $1/\sqrt{\varepsilon}$ (or macroscopic length $\sqrt{\varepsilon}$). Of course, (35) does not provide a complete set of macroscopic equations and without further information it is not clear whether or how the fluxes can be computed in a pointwise manner from the densities. The equations are nevertheless very useful since they allow us to derive and check partial information on the solution of the modulation equations from numerical data. In particular, in the context of modulated traveling waves, the PDEs (35a) and (35b) correspond to (31a) and (31b), respectively.

3.3 | Self-similar solutions

The Whitham modulation equations (31) are a system of conservation laws that can be compactly expressed in the form

$$\mathbf{P}(\mathbf{q})_T + \mathbf{Q}(\mathbf{q})_X = 0, \quad \mathbf{q} = [\bar{u}, a, k]^{\mathrm{T}}, \tag{36}$$

where the vectorial density $\mathbf{P}$ and flux $\mathbf{Q}$ depend on the slowly varying parameters $\mathbf{q}$ through integrals of the periodic orbit φ. Equation (36) can also be expressed in the form

$$\mathbf{q}_T + \mathcal{A}\mathbf{q}_X = 0, \quad \mathcal{A} = \left(\frac{\partial \mathbf{P}}{\partial \mathbf{q}}\right)^{-1} \frac{\partial \mathbf{Q}}{\partial \mathbf{q}}, \tag{37}$$

provided the inverse is nonsingular. We will use solutions of the Whitham equations to approximate the long-time dynamics of solutions to the Riemann problem (3), (4). Consequently, it is natural to consider the Riemann problem

$$\mathbf{q}(X, 0) = \begin{cases} \mathbf{q}_- & X < 0 \\ \mathbf{q}_+ & X > 0 \end{cases} \tag{38}$$

for the Whitham equations (36) themselves. Rarefaction (simple) wave solutions and discontinuous shock solutions of the binary oscillation modulation system (10) were used in Ref. 16 to interpret various features of the numerical solutions. In this work, we will make use of RW and discontinuous shock solutions of the more general Whitham modulation equations (31).

The invariance of the Riemann problem (36), (38) with respect to the hydrodynamic scaling $X \to \sigma X'$, $T \to \sigma T'$ for real $\sigma \neq 0$ suggests seeking self-similar solutions in the form $\mathbf{q} = \mathbf{q}(\xi)$, $\xi = X/T$. Equation (37) possesses RWs satisfying[48]

$$\frac{d\mathbf{q}}{d\xi} = \frac{\mathbf{r}_i}{\nabla\lambda_i \cdot \mathbf{r}_i}, \quad \mathbf{q}(\xi_\pm) = \mathbf{q}_\pm, \quad \xi_- < \xi_+, \tag{39}$$

where $\mathcal{A}\mathbf{r}_i = \lambda_i \mathbf{r}_i$ and $\lambda_i = \xi$, provided the characteristic field is genuinely nonlinear $\nabla\lambda_i \cdot \mathbf{r}_i \neq 0$. Since $\mathbf{q}_\pm$ lie on the same, one-dimensional integral curve, they are constrained by two integral relations resulting from integration of the third-order ODEs (39). Admissibility requires $\xi_- < \xi_+$. The eigenvalues λ_i can be interpreted as speeds. For example, in the context of DSWs, the trailing edge speed is $c_- = \xi_-$ and the leading edge speed $c_+ = \xi_+$.

Another class of self-similar solutions are discontinuous shock solutions to the Whitham system (31)

$$\mathbf{q}(\xi) = \begin{cases} \mathbf{q}_- & \xi < V \\ \mathbf{q}_+ & \xi > V, \end{cases} \tag{40}$$

where V is the velocity of the shock solution that satisfies the Rankine–Hugoniot jump conditions

$$-V[\![\mathbf{P}]\!] + [\![\mathbf{Q}]\!] = 0. \tag{41}$$

The brackets $[\![\cdot]\!]$ denote the jump in its argument evaluated on the left and right triple $\mathbf{q}_\pm$ that parameterize distinct, steady periodic orbits $\varphi_\pm$.

For strictly hyperbolic, genuinely nonlinear Whitham modulation equations with negative linear dispersion ($\partial_k^2\omega_0 < 0$), classical DSW solutions connecting the two constant states $u_\pm$ are described by a rarefaction solution of (39) in which $\lambda = \lambda_2$ is the middle characteristic speed and $\mathbf{q}_- = [u_-, 0, k_-]$, $\mathbf{q}_+ = [u_+, a_+, 0]$. The two constraints that result from integrating (39) determine the trailing edge wavenumber k_- and speed ξ_- as well as the leading edge amplitude a_+ and speed ξ_+.[5] Therefore, a classical DSW corresponds to an RW solution of the modulation equations, *not* a shock solution. For DSW construction, we will use the DSW fitting method, which leverages certain structural properties of the Whitham modulation equations under the assumptions of strict hyperbolicity and genuine nonlinearity in order to obtain k_-, a_+, and $\xi_\pm$ by integrating a scalar ODE.[5,49]

Whitham himself pondered the notion of discontinuous shock solutions to his eponymous equations.[1] But their utility was only recently discovered in Ref. 6 where shock solutions of the Whitham modulation equations for a fifth-order KdV (KdV5) equation were deemed admissible if there exists a heteroclinic traveling wave solution connecting the corresponding left and right periodic orbits, each moving with the same speed as the shock. Such traveling wave solutions are possible in higher-order equations such as KdV5. These *Whitham shocks* were used to solve the Riemann problem for KdV5 and, later, were investigated in the Kawahara equation.[50] In this paper, we will show that similar Whitham shocks emerge as the traveling wave portion of the TDSW solution in Figure 1. We also provide analytical and numerical evidence of the existence of a new class of Whitham shocks, that is, shock solutions of the Whitham modulation equations (31) whose corresponding left and right periodic orbits possess the same frequency but different speeds than one another and the shock itself (see US in Figure 1).

3.4 | Weakly nonlinear regime

In the previous sections, we derived the modulation equations supposing the existence of a family of nonlinear periodic solutions. In the case where no known explicit periodic solution is available, it is useful to approximate the periodic solution with a truncated cosine series. The approximation via the Poincaré–Lindstedt method utilizes an asymptotic expansion of both the profile of the periodic solution and its frequency in the small amplitude parameter $0 < a \ll 1$. The approximate periodic solution and its frequency are given, for a generic potential Φ by

$$u \sim \bar{u} + \frac{a}{2}\cos(kn - \omega t) + a^2 \frac{\sin(2k)\Phi^{(3)}(\bar{u})}{16\Phi''(\bar{u})(2\sin(k) - \sin(2k))}\cos(2(kn - \omega t)) + o(a^2), \tag{42}$$

$$\omega \sim \Phi''(\bar{u})\sin(k) + a^2\omega_2 + o(a^2), \quad \omega_2 = \frac{1}{32}\sin(k)\left(\frac{\Phi^{(3)}(\bar{u})^2}{(\sec(k) - 1)\Phi''(\bar{u})} + \Phi^{(4)}(\bar{u})\right), \tag{43}$$

which maintain their asymptotic ordering so long as

$$a^2/|k| \ll 1 \quad \text{and} \quad |a\Phi^{(3)}(\bar{u})/\Phi''(\bar{u})| \ll 1, \tag{44}$$

that is, for $\Phi(u) = u^3/3$, neither $|k|$ nor $|\bar{u}|$ are too small. Inserting (42), (43) into the modulation equations (31), we obtain the weakly nonlinear Whitham modulation equations in conservative form by retaining terms up to $O(a^2)$

$$\bar{u}_T + \left(\Phi'(\bar{u}) + \frac{a^2}{16}\Phi'''(\bar{u})\right)_X = 0, \tag{45}$$

$$\left(\Phi(\bar{u})+\frac{a^2}{16}\Phi''(\bar{u})\right)_T+\left(\frac{1}{2}\Phi'(\bar{u})^2+\frac{a^2}{16}\left(\Phi''(\bar{u})^2\cos(k)+\Phi'(\bar{u})\Phi'''(\bar{u})\right)\right)_X=0, \tag{46}$$

$$k_T+\left(\Phi''(\bar{u})\sin(k)+\frac{a^2}{32}\sin(k)\left(\frac{\Phi^{(3)}(\bar{u})^2}{(\sec(k)-1)\Phi''(\bar{u})}+\Phi^{(4)}(\bar{u})\right)\right)_X=0. \tag{47}$$

In the case of the cubic potential (13), our focus here, the modulation equations are

$$\bar{u}_T+\left(\bar{u}^2+\frac{a^2}{8}\right)_X=0, \tag{48a}$$

$$\left(\frac{\bar{u}^3}{3}+\frac{a^2}{8}\bar{u}\right)_T+\left(\frac{1}{2}\bar{u}^4+\frac{a^2}{8}\bar{u}^2(2\cos(k)+1)\right)_X=0, \tag{48b}$$

$$k_T+\left(2\bar{u}\sin(k)+\frac{a^2}{16}\left(\frac{\sin(k)}{(\sec(k)-1)\bar{u}}\right)\right)_X=0. \tag{48c}$$

Properties of the modulation equations can be elucidated by casting them in quasi-linear form $\tilde{\mathbf{q}}_t+\tilde{\mathcal{A}}\tilde{\mathbf{q}}_x=0$, where

$$\tilde{\mathcal{A}}=\begin{bmatrix}2\bar{u} & \frac{1}{8} & 0\\ 4a^2\cos(k) & 2\bar{u}\cos(k) & -2a^2\bar{u}\sin(k)\\ 2\sin(k)+a^2\omega_{2,\bar{u}} & \omega_2 & 2\bar{u}\cos(k)+a^2\omega_{2,k}\end{bmatrix},\qquad \tilde{\mathbf{q}}=\begin{bmatrix}\bar{u}\\ a^2\\ k\end{bmatrix}. \tag{49}$$

A perturbation calculation gives the eigenvalues of the flux matrix $\mathcal{A}$ to $\mathcal{O}(a)$

$$\lambda_3=2\bar{u}+O(a^2), \tag{50a}$$

$$\lambda_2=2\bar{u}\cos(k)+\frac{a}{2}\cos\left(\frac{k}{2}\right)\sqrt{2-\cos(k)}+O(a^2), \tag{50b}$$

$$\lambda_1=2\bar{u}\cos(k)-\frac{a}{2}\cos\left(\frac{k}{2}\right)\sqrt{2-\cos(k)}+O(a^2), \tag{50c}$$

with the corresponding right eigenvectors

$$\mathbf{r}_3=\left[\bar{u}\tan\left(\frac{k}{2}\right),0,1\right]^T+O(a^2), \tag{51a}$$

$$\mathbf{r}_2=\left[0,0,\sqrt{2-\cos(k)}\right]^T+\frac{a}{4}\left[\csc\left(\frac{k}{2}\right),-32\bar{u}\sin\left(\frac{k}{2}\right),0\right]^T+O(a^2), \tag{51b}$$

$$\mathbf{r}_1=[0,0,\sqrt{2-\cos(k)}]^T-\frac{a}{4}\left[\csc\left(\frac{k}{2}\right),-32\bar{u}\sin\left(\frac{k}{2}\right),0\right]^T+O(a^2). \tag{51c}$$

The quasi-linear system is strictly hyperbolic if all of the eigenvalues are distinct, and real-valued. To the order of the approximation given, the weakly nonlinear system is strictly hyperbolic

provided $a \neq 0$, $k \neq \pi$, and

$$|\overline{u}| \neq \overline{u}_{\mathrm{cr}}, \quad u_{\mathrm{cr}} = \frac{a \cos\left(\frac{k}{2}\right)\sqrt{2-\cos(k)}}{8\sin^2\left(\frac{k}{2}\right)}. \tag{52}$$

When $\overline{u} > u_{\mathrm{cr}}$ and $a > 0$, the eigenvalues are ordered $\lambda_1 < \lambda_2 < \lambda_3$. When $a = 0$, Equations (48a) and (48b) coincide with the Hopf equation for the mean $\bar{u}$ and the remaining equation corresponds to the conservation of waves from linear wave modulation theory. When $k = \pi$, Equation (48c) is identically satisfied. While intuition might suggest that (48a) and (48b) are somehow related to the modulation equations for binary oscillations (10), in fact, the asymptotic derivation breaks down. For example, the period average of the weakly nonlinear solution (42) is no longer $\bar{u}$ but rather $\bar{u} - \frac{a^2}{8\bar{u}}$ so that the density in (48a) does not correspond to the density in (35a). When $k = \pi$, one should discard Equation (48) altogether in favor of the modulation equations for binary oscillations (10), which apply beyond the weakly nonlinear regime considered here.

4 | CLASSIFICATION OF SOLUTIONS

From now onward, we focus solely on the discrete equation (3) (Equation 12 subject to 13). Figure 1 depicts seven qualitatively distinct solution families to the Riemann problem (3), (4) depending upon the parameters $u_{\pm}$ in the initial data. We now proceed to describe each of these solution families using a combination of numerical simulation, Whitham modulation theory, and quasi-continuum approximation. The straight-line boundaries between each solution family in Figure 1 are determined empirically (to two decimal digits accuracy) and some are explained by analytical considerations. By a possible reflection and unit shift of the lattice $n \to -n-1$ and a rescaling of time, we can, without loss of generality, set either $u_+ = 1$ while varying $u_- \in [-1, 1]$ or set $u_- = 1$ while varying $u_+ \in [-1, 1]$. Therefore, we can map out the phase diagram in the (u_-, u_+) plane by traversing the top and right edges of the square $[-1, 1]^2$.

The special case in which $u_+ = u_-$ is trivial but the case in which $u_+ = -u_- \neq 0$ is the SS solution (11) which, as already noted, is an expansion shock solution of the inviscid Burgers equation (1) or dispersionless limit equation for the mean (32) with characteristics that emanate from the discontinuity. Otherwise, the solutions exhibit more complexity, which we now explore. We start with the simplest case first, and then work toward the richest, most complex scenario.

4.1 | Rarefaction waves

The simplest observed dynamical structure is the rarefaction wave shown as RW in Figure 1. Empirically, we find that they form when $u_+ = 1$ and $u_- \in (0.18, 1)$. The bifurcation at $u_- = 0.18$ will be described in Section 4.5. The leading-order RW behavior is given by the self-similar solution ($\xi = n/t = X/T$)

$$u_n(t) \sim \bar{u}(\xi) = \begin{cases} u_- & \xi \leq 2u_- \\ \xi/2 & 2u_- < \xi \leq 2u_+ \\ u_+ & 2u_+ < \xi \end{cases} \tag{53}$$

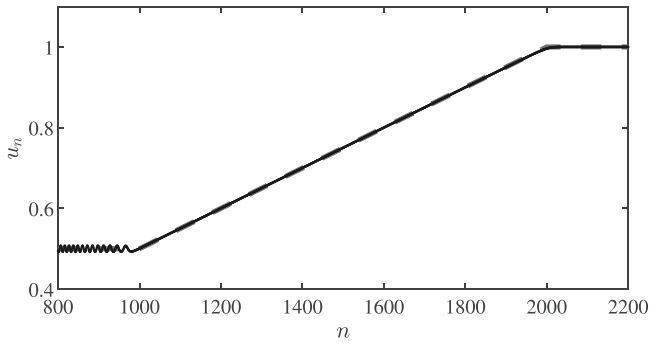

FIGURE 3 Comparison of the self-similar solution (53) (red dashed) with numerical simulation of the initial data (4) with $u_- = 0.5$ and $u_+ = 1$ (black dots).

of the dispersionless equation (32). A favorable comparison of this profile with a numerical simulation is shown in Figure 3. Because the data are expansive, the effect of dispersion manifests at higher order where a small amplitude, dispersive wavetrain is emitted from the lower, left edge of the RW. The slowest (most negative) group velocity is $\partial_k \omega_0(\pi, u_-) = -2u_-$, which corresponds to an inflection point of the linear dispersion relation (14). Consequently, the leftmost edge of these small amplitude waves is expected to have an Airy profile whose decay estimate is proportional to $t^{-1/3}$, similar to the Fourier analysis carried out for linear FPUT chains.[51] The details of the linear wavetrain accompanying RWs and DSWs for the BBM equation were studied in Ref. 7. We follow a similar procedure by linearizing about the left initial state $u_n = u_- + v_n$ to obtain

$$\frac{d}{dt} v_n + u_-(v_{n+1} - v_{n-1}) = 0. \tag{54}$$

The initial data (4) then become

$$f_n = \begin{cases} 0 & n < 0, \\ u_+ - u_- & n \geq 0, \end{cases} \tag{55}$$

whose discrete-space Fourier transform is the distribution

$$\hat{f}(k) = \sum_{n=-\infty}^{\infty} f_n \mathrm{e}^{-ink} = (u_+ - u_-)\left(\frac{1}{1 - \mathrm{e}^{-ik}} + \pi\delta(k) \right), \quad k \in (-\pi, \pi], \tag{56}$$

where $\delta(k)$ is the Dirac delta. To approximate the nonlinear equation (3) by the linear equation (54), one could seek solutions in which $0 < u_+ - u_- \ll |u_+| + |u_-|$. Alternatively, we follow Ref. 7 and consider scale separation in which the highest frequency components of (56) are assumed to separate from the RW so that the initial data become

$$\hat{v}(k, 0) = \begin{cases} \dfrac{u_+ - u_-}{1 - \mathrm{e}^{-ik}} & k_0 < |k| \leq \pi, \\ 0 & \text{else} \end{cases} \tag{57}$$

for some $0 < k_0 < \pi$ that is sufficiently far from the zero dispersion points, $k = 0, \pi$. Then, the solution of the linear equation (54) can be determined by taking the discrete-space Fourier transform $\hat{v}(k, t) = \sum_n v_n(t)\mathrm{e}^{-ink}$. The solution of Equation (54) subject to (57) is

$$v_n(t) = \frac{1}{2\pi} \int_{-\pi}^{\pi} \hat{v}(k, 0) \mathrm{e}^{i\theta(k)t} \, dk \qquad \theta(k; n, t, u_-) = kn/t - 2u_- \sin(k). \tag{58}$$

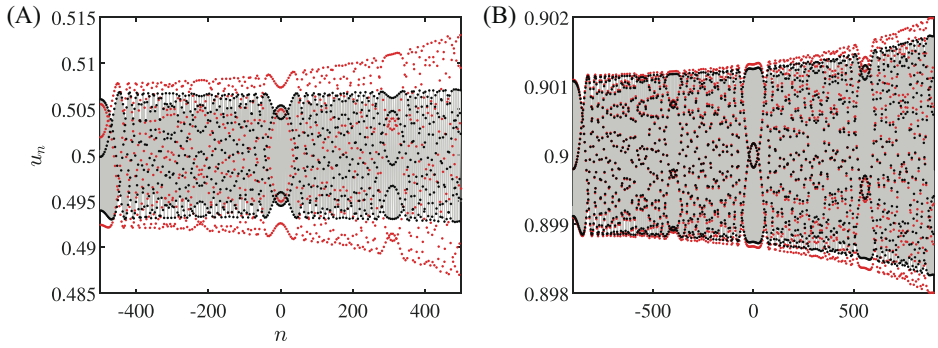

FIGURE 4 Comparison of the linear wave from the stationary phase analysis (60) (red dots) and numerical simulation (black dots) resulting in a rarefaction wave for (A) $u_- = 0.5$ and (B) $u_- = 0.9$.

Quantitative information regarding the solution can be determined asymptotically for $t \to \infty$ with n/t fixed using the method of stationary phase.[1] The leading-order behavior is determined by analyzing the integral (58) near the stationary points, k_s where $\theta_k(k_s) = 0$. Stationary points are therefore given by $\pm k_s$ where

$$n/t = 2u_- \cos(k_s) \tag{59}$$

for $-2u_- < n/t < 2u_-$. The leading-order behavior in the vicinity of the stationary points is determined by expanding the integrand in (58) about the stationary points $k = \pm k_s$. When $k_s \neq \pi$ and $|k_s| > k_0$, the leading-order behavior is

$$\begin{aligned} v_n(t) &\sim \frac{1}{\sqrt{2\pi t|\partial_k^2 \omega_0(k_s, u_-)|}} \left(\hat{v}(k_s, 0) e^{ik_s n - i\omega_0(k_s, u_-)t + i\pi/4} + \text{c.c.}\right), \\ &= \frac{1}{\sqrt{2\pi t|\partial_k^2 \omega_0(k_s, u_-)|}} (u_+ - u_-) \csc\left(\frac{k_s}{2}\right) \sin\left(\theta(k_s)t + \pi/4 + \frac{k_s}{2}\right). \end{aligned} \tag{60}$$

The profile (60) is compared with numerical simulations of the initial-value problem in Figure 4 on the interval $[-u_- t_f, u_- t_f]$ at a final simulation time of $t = t_f = 1000$. The interval is chosen so that $k_s \in (\pi/3, 2\pi/3)$, that is, the truncation parameter $k_0 = \pi/3$ and we avoid the degenerate stationary points $k_s = 0, \pi$. We observe that the linear profile (60) is in good agreement with the numerical simulation. However, for larger initial jumps, the linear wave begins to deviate from the simulation. This may be attributed to the emergence of stronger nonlinear effects not captured by the leading-order asymptotics which require a larger truncation parameter k_0.

To investigate the leftmost edge of the linear wave emitted from the RW, we modify our previous analysis and expand the phase in the integral (58) about the inflection point $k = \pi$ of the linear dispersion relation

$$\theta(k) \sim \pi n/t - (n/t + 2u_-)(\pi - k) + u_-(\pi - k)^3/3 + \cdots \tag{61}$$

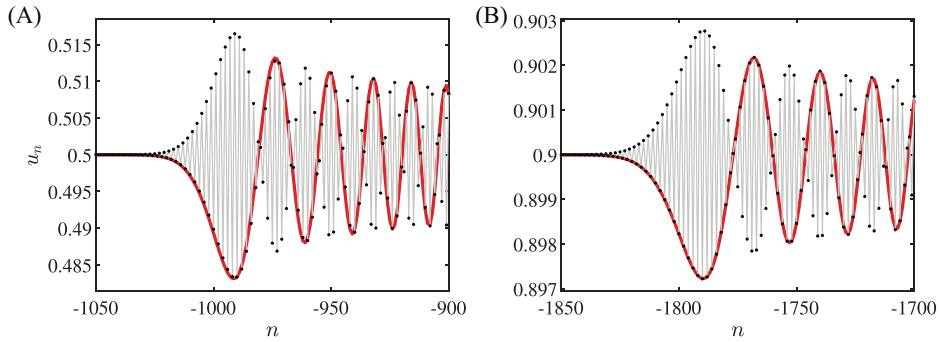

FIGURE 5 Comparison of the Airy profile (62) (red curve) with numerical simulations (black dots) resulting in a rarefaction wave with initial data $u_+ = 1$ and (A) $u_- = 0.5$ and (B) $u_- = 0.9$.

The expansion (61) is inserted into the integral (58). A calculation reveals that the leading-order asymptotics in the vicinity of the ray $n/t = -2u_-$ are given by

$$v_n(t) \sim -\frac{u_+ - u_-}{2(tu_-)^{1/3}} \cos(\pi n) \mathrm{Ai}\big(-(n + 2tu_-)(tu_-)^{-1/3}\big), \tag{62}$$

where $\mathrm{Ai}(\cdot)$ is the Airy function $\mathrm{Ai}(z) = \frac{1}{2\pi} \int_{\mathbb{R}} \mathrm{e}^{i\kappa z + i\kappa^3/3}\, d\kappa$. The Airy profile (62) favorably compares with the two Riemann problem simulations depicted in Figure 5, even for large $u_+ - u_-$.

It is worth contrasting the observed RW dynamics with those of the quasi-continuum approximation in the BBM equation (8) that was studied in Ref. 7. Qualitatively, the dynamics exhibited by the two models in overlapping regimes of the (u_-, u_+) plane of Riemann data are very similar. Both equations exhibit large-scale dynamics that are well-approximated by the self-similar solution (53) and its analog for the BBM equation. The details of the short-scale, emitted dispersive wavetrains are quantitatively different but, since both equations admit nonconvex linear dispersion relations, they both exhibit Airy profiles with amplitude decay proportional to $t^{-1/3}$.

The long-time dynamics produced by the lattice model (3) significantly differs from those generated by its quasi-continuum BBM counterpart (8) when either equation is strongly influenced by small-scale effects. The actual Riemann problems for the BBM equation studied in Ref. 7 were tanh-smoothed, monotone transitions between u_- and u_+, a feature which introduces an external length scale characterizing the width of the initial transition. When this width is larger than the $\mathcal{O}(1)$ oscillatory length scale (or $\mathcal{O}(\varepsilon)$ in Equation 8), the BBM equation exhibits an RW for all $|u_-| < u_+$. As shown in Figure 1, RW generation on the lattice is limited to the region $0.18u_- < u_+ < u_-$, $u_- > 0$, with short-scale oscillatory dynamics occurring when $-u_- < u_+ < 0.18u_-$, $u_- > 0$. When the BBM initial transition width is sufficiently small, RW generation can be accompanied by the spontaneous generation of solitary waves and/or an expansion shock, features not observed in the lattice model.

4.2 | Dispersive shock waves

For $u_- = 1$ and $u_+ \in (0, 1)$, the data are compressive and results in an expanding, modulated oscillatory wavetrain between the states u_- and u_+. This structure is called a DSW; see the panel labeled DSW in Figure 1. In Ref. 30, DSWs were studied in Equation (35) with $\Phi(u) = u^2/2 + u^4/4$

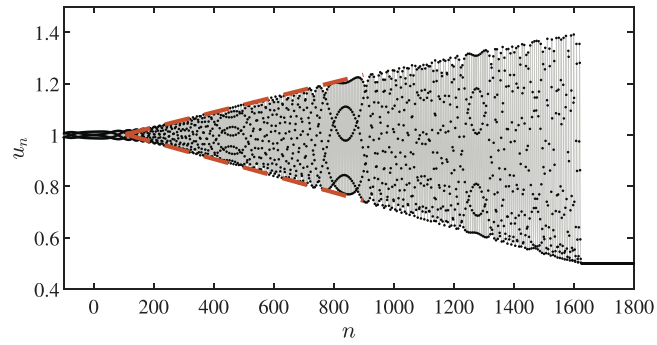

FIGURE 6 Discrete dispersive shock wave (DSW) for $u_- = 1$, $u_+ = 0.5$ at $t = 1000$. The dashed red oscillatory envelope curves intersect at the harmonic edge.

and $u_- = 1$, $u_+ = 0$ using numerical simulations and a dimension reduction approach. In the following, we study DSWs in the system (3) as the step value u_+ varies using two semianalytical approaches, DSW fitting and a continuum model.

4.2.1 | Approximation of the DSW harmonic and soliton edge speeds via DSW fitting

In this section, we outline the method for fitting the macroscopic DSW properties (edge speeds, amplitudes, and wavenumbers) by applying the fitting method first introduced by El[49]; see also Ref. 5. This method was originally developed and justified for continuum PDEs where it has been extensively applied. Since it only requires knowledge of the linear dispersion relation and the solitary wave amplitude–speed relation, it is straightforward to extend the method to the semidiscrete lattice equation (12).

An example DSW from a numerical simulation of the Riemann problem with $u_+ = 0.5$ and $u_- = 1$ is shown in Figure 6. The DSW is comprised of a modulated, nonlinear wavetrain that terminates in two distinct limits: vanishing amplitude (called the harmonic edge) and vanishing wavenumber (called the soliton edge). The modulation solution describing the DSW is the rarefaction solution (39) of the Whitham modulation equations (31) with $\mathbf{q}_- = [u_-, 0, k_-]^T$, $\mathbf{q}_+ = [u_+, a_+, 0]^T$. The harmonic edge wavenumber k_- and the soliton edge amplitude a_+, as well as their corresponding edge speeds ξ_- and ξ_+ are determined by integrating the ODE (39), thus relating these macroscopic DSW properties to the initial data $u_\pm$. In numerical simulations, the amplitude of the DSW does not vanish exactly at the harmonic edge, so we define the location of the trailing edge by the intersection of the oscillatory envelope curves shown in Figure 6.

Although the DSW modulation is determined, in principle, by the aforementioned rarefaction solution of the Whitham modulation equations (assuming strict hyperbolicity and genuine nonlinearity of the second characteristic field), we do not have explicit expressions relating the integrals in (31) to the periodic orbit's parameters $\mathbf{q} = [\bar{u}, a, k]^T$. An alternative technique that allows one to obtain the DSW's edge properties is the DSW fitting method.[5] This method assumes the existence of the rarefaction solution. For the sake of completeness, we will carry out the DSW fitting procedure for a generic potential $\Phi(u)$. The wavenumber of the DSW at the harmonic edge can be determined by solving the initial-value problem

$$\frac{dk}{d\bar{u}} = \frac{\partial_{\bar{u}}\omega_0(k,\bar{u})}{\Phi''(\bar{u}) - \partial_k\omega_0(k,\bar{u})} = \frac{\Phi'''(\bar{u})\sin k}{\Phi''(\bar{u})(1-\cos k)}, \quad k(u_+) = 0, \tag{63}$$

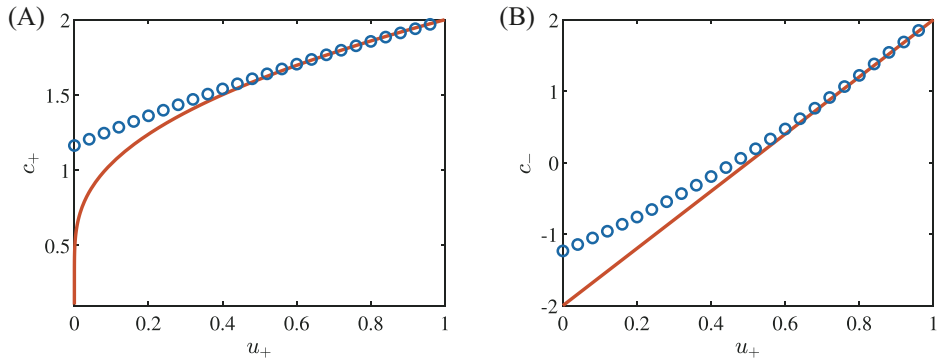

FIGURE 7 Comparison of dispersive shock wave (DSW) fitting predictions (solid, red line) and numerical simulations of DSWs with $u_- = 1$ (blue circles). The leading edge, solitary wave velocity c_+ is shown in panel (A) and the trailing, linear wave edge velocity comparisons are shown in panel (B).

where ω_0 is the linear dispersion relation (14). This ODE can be integrated by separation of variables to obtain

$$k(\bar{u}) = \cos^{-1}\left(\frac{2\Phi''(u_+) - \Phi''(\bar{u})}{\Phi''(\bar{u})}\right). \tag{64}$$

The wavenumber at the DSW harmonic edge is $k_- = k(u_-)$. The velocity of the harmonic edge is given by evaluating the linear group velocity at k_-

$$c_- = \partial_k \omega_0(k_-, u_-) = 2\Phi''(u_+) - \Phi''(u_-). \tag{65}$$

The velocity of the DSW at the soliton edge is calculated in a similar way. We begin by introducing the conjugate variables $\tilde{\omega}_0\left(\tilde{k}, \bar{u}\right) = -i\omega_0(i\tilde{k}, \bar{u}) = \Phi''(\bar{u})\sinh(\tilde{k})$, where $\tilde{k}$ acts as a soliton amplitude parameter. The velocity of the DSW soliton edge is deduced by evaluating the solitary wave dispersion relation $c_+ = \tilde{\omega}(\tilde{k}_+, u_+)/\tilde{k}_+$, where we find $\tilde{k}_+$ by solving the initial-value problem

$$\frac{d\tilde{k}}{d\bar{u}} = \frac{\partial_{\bar{u}}\tilde{\omega}_0}{\Phi''(\bar{u}) - \partial_{\tilde{k}}\tilde{\omega}_0} = \frac{\Phi'''(\bar{u})\sinh\tilde{k}}{\Phi''(\bar{u})(1-\cosh\tilde{k})}, \qquad \tilde{k}(u_-) = 0. \tag{66}$$

Integration results in

$$\tilde{k}(\bar{u}) = \cosh^{-1}\left(\frac{2\Phi''(u_-) - \Phi''(\bar{u})}{\Phi''(\bar{u})}\right), \tag{67}$$

and the soliton edge conjugate wavenumber $\tilde{k}_+ = \tilde{k}(u_+)$. The soliton edge velocity of the discrete DSW is given by

$$c_+ = \frac{\tilde{\omega}(\tilde{k}_+, u_+)}{\tilde{k}_+} = \frac{2}{\tilde{k}_+}\sqrt{\Phi''(u_-)(\Phi''(u_-) - \Phi''(u_+))}. \tag{68}$$

Comparisons with numerical simulations of the Riemann problem are given in Figure 7 with the potential $\Phi(u) = u^3/3$ and the initial data normalized so that $u_- = 1$. To estimate the velocity of the leading edge, we track the position of the rightmost lattice site that is above the far-field initial data u_+ at the integer valued times in our numerical simulation. This time-series data are fit

with a line whose slope is the approximate velocity of the soliton edge of the DSW. To estimate the harmonic edge velocity, we produce a linear fit of the modulated wavetrain amplitude near the location of the harmonic edge, which is found by extracting peaks of the solution at output times. The intersection of this linear approximation with the constant level u_- is the approximate location of the DSW harmonic edge. The time interval of our numerical computations varies depending on u_+. For instance, when we take $u_+ = 0.1$, we approximate the solution at $t \approx 1000$, while taking $u_+ = 0.9$ requires the longer time $t \approx 4000$ for the solution to asymptotically develop. Upon varying u_+, we observe good agreement between the predictions of DSW fitting for the DSW harmonic and soliton edge velocities and numerical simulations for $u_+ \gtrsim 0.5$, while the predictions begin to deviate from what is observed in numerical simulations below this threshold. The DSW fitting method is subject to the convexity conditions

$$\frac{\partial c_\pm}{\partial u_-} \neq 0, \quad \frac{\partial c_\pm}{\partial u_+} \neq 0. \tag{69}$$

A direct calculation for the potential $\Phi(\bar{u}) = \bar{u}^3/3$ demonstrates that these convexity conditions are indeed satisfied. The numerical results suggest that the DSW fitting method provides an adequate approximate prediction of the discrete DSW edge properties.

The harmonic edge of the DSW is accompanied by linear radiation much like the left edge of the RW in the previous section. To describe this, we apply the same approach as in Section 4.1 to approximating the small amplitude linear waves that emanate from the DSW's harmonic edge. The only change is that, for the DSW, $u_+ - u_- < 0$ in Equation (55). A comparison is shown in Figure 8.

4.2.2 | Approximations of the leading edge amplitude via a quasi-continuum model

In this subsection, we go a bit deeper into the description of the solitary wave at the soliton edge of the DSW. Like in the previous subsection, for $u_+ \in (0, 1)$ (where $u_- = 1$ is fixed), we numerically solve the Riemann problem, generate a DSW, and extract the amplitude of the soliton edge, and its speed. This is done by inspecting the time series of a node sufficiently far from the center of the lattice (we chose $n = 300$, in which case we have observed the leading edge is developed) and simply computing the amplitude as $a_+ = \max u_n(t) - u_+$. The speed is estimated by computing $c_+ = 1/(t_{n+1} - t_n)$ where t_n and t_{n+1} are the time values where u_n and u_{n+1} attain their maxima. The blue open circles in Figure 9A show the amplitude of the DSW soliton edge as a function of u_+. Since for each value of u_+, we compute both the speed c_+ and amplitude a_+, we also show a parametric plot of (c_+, a_+) parameterized by u_+ in Figure 9B.

To confirm that the DSW soliton edge is indeed described by a solitary wave, we compute a numerical solitary wave solution of the lattice equation (12) by using a fixed-point iteration scheme[32] to solve the advance delay equation

$$2c\mathcal{V}'(\eta) = \Phi'(u_+ + \mathcal{V}(\eta + 1)) - \Phi'(u_+ + \mathcal{V}(\eta - 1)), \tag{70}$$

which is a rescaled copy of (18) and obtained by substituting

$$u_n(t) = u_+ + \mathcal{V}(\eta), \qquad \eta = n - ct \tag{71}$$

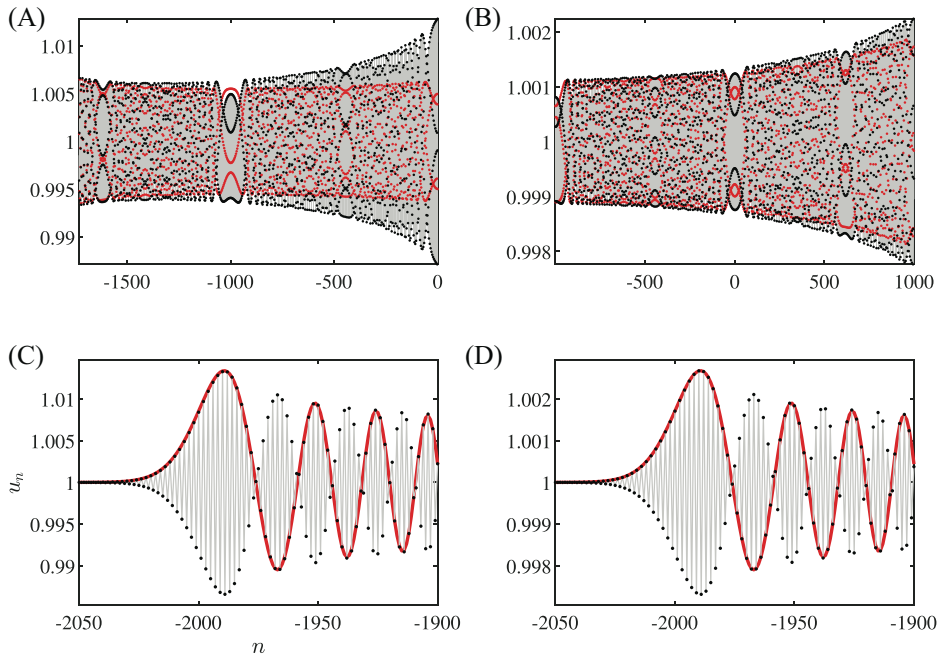

FIGURE 8 Comparison of stationary phase analysis (60) and the Airy profile (62) (both in red) with numerical simulations (black dots) resulting in a dispersive shock wave (DSW) at $t = 1000$ with initial data $u_- = 1$ and (A, C) $u_+ = 0.5$ and (B, D) $u_+ = 0.9$. The band-limited interval of the stationary points in the formula (60) are (A) $k_s \in (2\pi/3, 5\pi/6)$ and (B) $k_s \in (\pi/3, 2\pi/3)$. These intervals are chosen to avoid the linear waves at the left edge of the DSW.

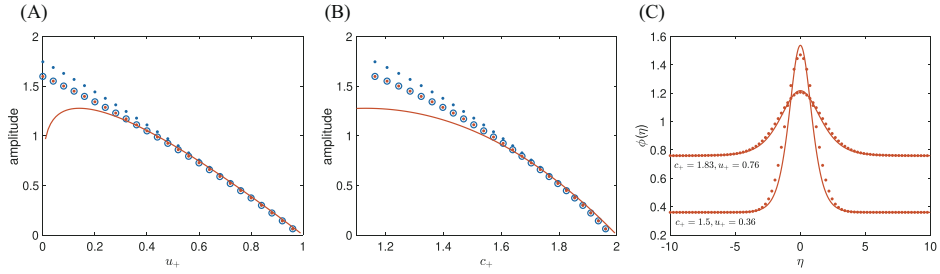

FIGURE 9 (A) Amplitude of the DSW soliton edge as a function of u_+ for the numerical simulation (open blue circles), the numerical solitary wave amplitude (solid red dots), the quasi-continuum formula $\frac{3c_+}{2} - 3u_+$ (solid blue dots, with the c_+ obtained numerically), and the analytical prediction given by Equation (74) (red line). (B) Same as panel (A), but the amplitude is shown against the wave speed $c = c_+$. (C) Comparison of the numerical solitary wave (solid red dots) and the quasi-continuum approximation given by Equation (73).

into Equation (12). While we are free to select values of c and u_+ when solving Equation (70), we select combinations of them according to the relationship extracted from the DSW soliton edge (i.e., the blue circles in Figure 9A). Upon convergence of the scheme, we compute the amplitude of the resulting solitary wave, which is the maximum of the wave minus the background u_+. The amplitudes of the solitary waves are shown as the solid red dots in Figure 9A,B. Note that these

red dots fall almost exactly within the blue circles, indicating that the soliton edge of the DSW is indeed well-approximated by a solitary wave solution of the lattice equation.

We can obtain an analytical approximation of discrete solitary waves by considering the BBM quasi-continuum approximation (8) of the lattice dynamics (3). Entering the moving frame $U(X,T) = \phi(X - cT)$ and integrating once, this PDE becomes the second-order ODE

$$c\frac{\varepsilon^2}{6}\phi'' = B + c\phi - 2\phi^2, \tag{72}$$

where B is an arbitrary integration constant. This ODE can be solved using quadrature.[52] In particular, the solitary wave with tails decaying to the background state u_+ has the form

$$u_n(t) = \phi(X - cT) = u_+ + \left(\frac{3c}{2} - 3u_+\right)\operatorname{sech}^2\left(\sqrt{\frac{\frac{3}{2}c - 3u_+}{c}}(n - ct)\right), \tag{73}$$

which assumes $c > 2u_+$. Note the maximum speed of linear waves on a background u_+ is $2u_+$, implying the solitary waves travel faster than all linear waves, as expected. In Equation (73), c and u_+ can be chosen independently of each other but we once again select combinations of them according to the relationship extracting from the DSW soliton edge (the blue circles in Figure 9A). The solid blue dots of Figure 9A show the quasi-continuum prediction of the amplitude $a_+ = \frac{3c_+}{2} - 3u_+$, where it is seen that the approximation becomes better as the jump height decreases (i.e., as $u_+ \to 1$). The quasi-continuum prediction of the amplitude is only semianalytical as it relies on the numerically obtained relationship of u_+ and c_+ from the DSW soliton edge data. An analytical prediction can be derived by using the DSW soliton edge speed in Equation (68) of the previous subsection, which allows us to express the amplitude, a_+, of the DSW soliton edge in terms of just u_+ (or c_+):

$$a_+ = \frac{6\sqrt{1 - u_+}}{\cosh^{-1}\left(\frac{2-u_+}{u_+}\right)} - 3u_+. \tag{74}$$

See the solid red line of Figure 9A,B for a plot of this formula.

Finally, the solitary wave profile given by Equation (73) matches the numerically computed solitary wave solution of Equation (70) quite well, especially for longer wavelength solutions. See Figure 9C for a comparison of the actual solitary wave (solid red dots) and quasi-continuum approximation (solid red line) for two example parameter sets.

Because, the quasi-continuum approximation of DSWs here and in Ref. 30 performs well, we briefly contrast the Riemann problems that result in DSWs for the lattice (3) and BBM (8) equations. The DSW fitting technique was applied to the BBM Riemann problem in Ref. 7. To compare our results for the lattice with DSWs in the BBM equation (8), we consider the initial transition occurring between $u_- = 1$ and $u_+ = 1 - \Delta$ for $0 < \Delta \ll 1$. At the DSW harmonic edge, the characteristic wavenumber $\varepsilon^2 K_-^2 = 4\Delta + 26\Delta^2/9 + \cdots$ and speed $C_- = 2 - 4\Delta + 14\Delta^2/9 + \cdots$ for BBM agree to $\mathcal{O}(\Delta)$ with the expansions $k_-^2 = 4\Delta + \frac{4}{3}\Delta^2 + \cdots$ and $c_- = 2 - 4\Delta$ for the lattice. Similarly, at the DSW soliton edge, the conjugate wavenumber $\varepsilon^2\tilde{K}_+^2 = 4\Delta + 10\Delta^2/9 + \cdots$ and speed $C_+ = 2 - 2\Delta/3 - 2\Delta^2/27 + \cdots$ agree to $\mathcal{O}(\Delta)$ with the lattice: $\tilde{k}_+^2 = 4\Delta + 8\Delta^2/3 + \cdots$ and $c_+ = 2 - 2\Delta/3 - 8\Delta^2/45 + \cdots$. The DSW's soliton edge amplitude in BBM is $A_+ = 2\Delta - \Delta^2/9 + \cdots$ whereas the prediction (74) for the lattice expands as $a_+ = 2\Delta - 4\Delta^2/15 + \cdots$. Note that to

leading order, these predictions agree with the DSW edge characteristics of the KdV equation $U_T + 2UU_X + \frac{1}{3}\varepsilon^2 U_{XXX} = 0$ for $X = \varepsilon n$, $T = \varepsilon t$, $U(X,T) = u_n(t)$. This is expected because BBM and KdV are asymptotically equivalent to leading order in the weakly nonlinear, long-wavelength regime.

In summary, the quasi-continuum approximation of lattice DSWs by DSWs in the BBM equation performs well for small initial jumps $0 < \Delta \ll 1$ when the oscillation wavelengths are much larger than the lattice spacing. The agreement to $\mathcal{O}(\Delta)$ in the DSW properties is expected and, in fact, is a statement of universality of the KdV equation as a weakly((nonlinear, long-wavelength model of dispersive hydrodynamics.[5] For sufficiently large Δ, the BBM DSW develops two-phase modulations near the trailing edge.[7] In contrast, for $\Delta > 1$, the lattice DSW bifurcates into a partial DSW connected to a traveling wave called a TDSW or exhibits blowup that we will describe in Sections 4.4 and 4.6, respectively.

4.3 | DSW + SS + RW

In this section, we investigate the case where the initial step generates two unsteady waves: a leftward-moving DSW and a right-moving RW. At the origin, there is an SS joining symmetric states at the level $u_n = \pm u_0$. A numerically computed example is depicted in Figure 10. This class of solutions is empirically found for $u_+ = 1$ and $u_- \in (-1, -0.26)$. As will be shown, the bifurcation at $u_- = -0.26$ occurs when the DSW's harmonic edge exhibits zero velocity.

The numerical simulation shown in Figure 10 suggests that the solution can be approximated for large t as

$$u_n(t) = \begin{cases} u_- & n \le s_- t \\ u_{\mathrm{DSW}}(n,t) & s_- t < n \le s_+ t \\ -u_0 & s_+ t < n \le 0 \\ u_0 & 0 < n \le 2u_0 t \\ u_{\mathrm{RW}}(n,t) & 2u_0 t < n \le 2u_+ t \\ u_+ & u_+ t < n. \end{cases} \tag{75}$$

The velocities $s_- < s_+$ give the motion of the DSW's soliton and harmonic edges, respectively. Across all of the simulations performed, we found the following relation for the intermediate, symmetric states $\pm u_0$ to hold to very high precision

$$u_0 = \frac{u_+ - u_-}{2}. \tag{76}$$

This relation implies that the DSW and RW have the same jump height, albeit with opposite polarities. We have been unable to mathematically justify this formula. However, as we show in Section 5, the value of the intermediate state u_0 depends strongly on particular details of the initial data. If the value of $u_0(0)$ is changed, then the intermediate value u_0 differs from (76).

Utilizing the formula (76), we can completely determine the velocities that divide the approximate solution (75) into different wave patterns. To determine the DSW edge velocities, we use Equations (65) and (68), which were derived under the assumption that $u_- > u_+ > 0$. In the case of the solution (75), the left (u_-) and right ($-u_0$) states are both negative. Since the governing

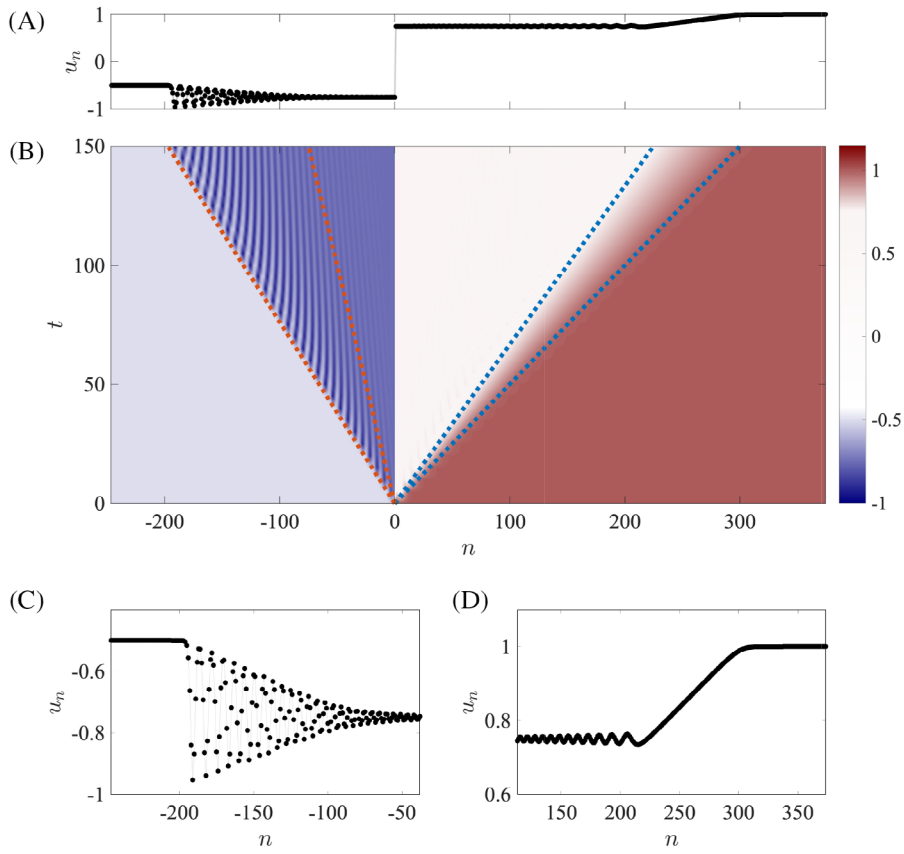

FIGURE 10 (A) An example dispersive shock wave + stationary shock + rarefaction wave (DSW + SS + RW) solution of the Riemann problem at $t = 500$ for $u_- = -0.5$, $u_+ = 1$. (B) Solution contour plot in the space-time plane with the predicted edge velocities of the DSW and RW denoted by dashed lines. (C) Zoom-in of DSW. (D) Zoom-in of RW.

equation (3) is invariant under the transformation $u_n(t) \to -u_{-n}(t)$, the DSW velocities are mapped as follows:

$$s_-(u_-, -u_0) = -c_+(u_0, -u_-), \quad s_+(u_-, -u_0) = -c_-(u_0, -u_-). \tag{77}$$

Then, using (76), we find

$$s_- = -\frac{2}{\cosh^{-1}(u_+/|u_-|)}\sqrt{u_+^2 - u_-^2}, \quad s_+ = 3u_- + u_+. \tag{78}$$

Figure 10B shows good agreement between the predicted velocities of the approximate solution (75) and a numerical simulation when $u_+ = 1$, $u_- = -0.5$.

The DSW remains detached from the SS so long as the harmonic edge velocity s_+ remains negative. From Equation (78), we predict that the DSW is no longer detached from the SS when $3u_- + u_+ = 0$, which, for $u_+ = 1$, occurs when $u_- = -\frac{1}{3}$. As noted earlier, the bifurcation from the DSW + SS + RW to the US case is empirically identified as occurring when $u_- = -0.26$. As shown

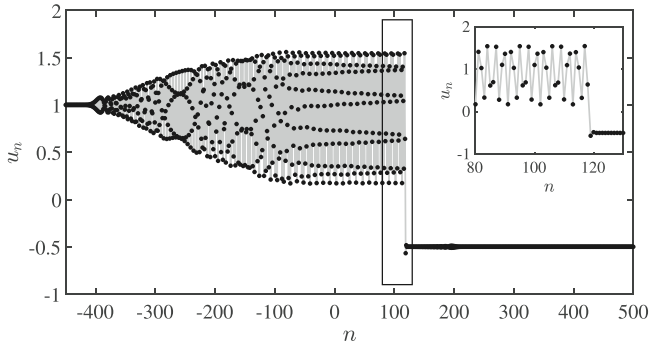

FIGURE 11 Example traveling dispersive shock wave (TDSW) that emerges from the initial data (4) with $u_- = 1$ and $u_+ = -0.5$ at $t = 200$. The inset is a zoom-in of the boxed region, showing details of the periodic-to-equilibrium traveling wave at the leading edge.

in Figure 10B, this small discrepancy in the bifurcation value can be explained by the deviation of the computed DSW harmonic edge velocity from the DSW fitting prediction (65).

4.4 | Traveling dispersive shock wave

In this section, we consider the case where a partial DSW connects the level behind, u_-, to a periodic-to-equilibrium traveling wave solution to the level ahead u_+. Although we do not directly compute it as a traveling wave solution of the discrete equation, it is interpreted as a heteroclinic connection between a periodic orbit with the constant level ahead u_+ based on an analysis of the numerical simulations of the Riemann problem. Such heteroclinic solutions of continuum equations with higher (fifth)-order dispersion were studied in Refs. 6, 50 and were associated with so-called TDSWs that emerge from an associated Riemann problem. The existence of a heteroclinic traveling wave solution to the governing PDE was identified as the admissibility criterion for a suitable discontinuous, shock solution of the Whitham modulation equations. Here, we use a similar admissibility criterion for a shock solution of the Whitham modulation equations (31): the existence of a heteroclinic traveling wave solution of the discrete conservation law (3).

For $u_- = 1$ and $u_+ \in (-0.724, 0)$, numerical simulations show a qualitatively similar solution pattern to that depicted in Figure 11 in which $u_n(t)$ begins on the left with the value u_-. It then progresses into an oscillatory wavetrain with increasing amplitude that resembles the leftmost portion of a DSW, called a partial DSW, that is then connected to a periodic traveling wave. The periodic traveling wave is connected to the constant state ahead u_+ via an abrupt transition that moves with the same speed. Collectively, this partial DSW and traveling wave is referred to as the traveling DSW.

The TDSW solution studied here is the discrete analog of the TDSW studied for the KdV5 equation.[6] The terminology *traveling dispersive shock wave* unites the unsteady component of the partial DSW and the steady traveling wave component (a heteroclinic periodic-to-equilibrium solution) to which it is attached in this nonclassical DSW. Consequently, the entire TDSW structure is unsteady.

4.4.1 | Approximation of the traveling wave via the quasi-continuum model

One can describe the periodic portion of the traveling wave (TW) (see, e.g., the interval $n \in [-90, 100]$) of Figure 11) using the continuum reduction presented in Section 4.2.2. In particular,

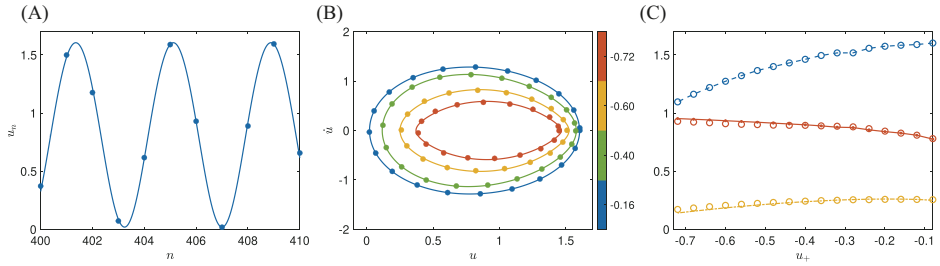

FIGURE 12 (A) Zoom of the periodic wave in the gray shaded region of Figure 11A with $u_+ = -0.16$ (blue markers) and quasi-continuum approximation (solid blue line). (B) Plot of the phase plane $(u_n(t), \dot{u}_n(t))$ for a time interval such that the periodic wave has developed. The color intensity corresponds to the value of u_+. Since the interval containing the traveling wave changes as u_+ is changed, the value of n for each loop is not fixed. In particular, $u_+ = -0.16$ (blue, $n = 400$), $u_+ = -0.40$ (green, $n = 400$), $u_+ = -0.6$ (yellow, $n = 140$), and $u_+ = -0.72$ (red, $n = 140$). The solid lines are the corresponding quasi-continuum approximations. (C) Plot of the mean (red solid lines), amplitude (blue dashed lines), and frequency $1/T$ (yellow dashed-dot line) as a function of u_-. The quasi-continuum approximation of these wave parameters is shown as open circles. For $u_+ \in [-0.72, -0.28]$, the lattice index is fixed to $n = 140$ and for $u_+ \in (-0.28, -0.2]$ to $n = 400$ and for $u_+ = 0.08$ to $n = 500$.

there is a three-parameter family of traveling wave solutions of the quasi-continuum BBM equation (8), given by

$$u_n(t) = r_1 + r_2 - r_3 + 2(r_3 - r_1)\mathrm{dn}^2\left(\sqrt{\frac{2(r_3 - r_1)}{c}}(n - ct), m\right),$$
$$m = \frac{r_2 - r_1}{r_3 - r_1}, \quad c = \frac{2(r_1 + r_2 + r_3)}{3}. \tag{79}$$

We treat r_1, r_2, r_3 as fitting parameters. After a sufficiently long time, the traveling wave in the numerical simulation forms, as in Figure 11. We then isolate a small interval of that traveling wave, which is then fit to Equation (79). Figure 12A shows a comparison of the actual lattice dynamics at $t = 480$ (blue markers) and quasi-continuum approximation (blue lines) with the step values $u_- = 1$ and $u_+ = -0.16$. Figure 12B shows the trajectory in the phase plane $(u_{400}(t), \dot{u}_{400}(t))$ (two outermost lobes) and $(u_{140}(t), \dot{u}_{140}(t))$ (two innermost lobes) for various values of u_- for the actual lattice dynamics (markers) and quasi-continuum approximation (lines). We show the phase plane for different values of n since the location of the traveling wave within the lattice is moving. The agreement is quite good throughout the interval of existence for these structures, but is best when the jump height is smallest (compare the blue and red trajectory of Figure 12B). The comparison of the frequency, amplitude, and mean parameters is shown in Figure 12C. These are computed via the following formulas with n fixed. For $u_- \in [-0.72, -0.28]$, the lattice index is fixed to $n = 140$, for $u_- \in (-0.28, -0.2]$, the index is $n = 400$, and for $u_- = 0.08$, the index is $n = 500$. The frequency is $f = 1/T$, where T is the period (computed as the peak-to-peak time of the trajectory); the mean is

$$\overline{u} = \frac{1}{T}\int_{I_T} u_n(t)\, dt,$$

where I_T is the time interval of one oscillation period. For the computations shown here, it is $I_T = [480 - T, 480]$. The amplitude is

$$a = \max_{t \in I_T} u_n(t) - \min_{t \in I_T} u_n(t).$$

Once the best-fit values of r_1, r_2, r_3 are obtained, the wave parameters can be computed directly from Equation (79) as

$$f = \frac{\sqrt{2c(r_3 - r_1)}}{2K(m)}, \quad \overline{u} = r_1 + r_2 - r_3 + 2(r_3 - r_1)\frac{E(m)}{K(m)}, \quad a = 2(r_2 - r_1),$$

where $K(m)$ and $E(m)$ are the complete elliptic integrals of the first and second kind, respectively. We note that while Equation (8) is able to describe the local periodic traveling wave dynamics of the TDSW structure, it does not admit continuous solutions resembling the entire TDSW structure since heteroclinic periodic-equilibrium solutions do not exist for the planar ODE (72). We note in passing that while discontinuous solutions of the BBM equation have been studied,[53] their direct connection to the TDSW solution is not yet apparent. Such a description may be possible by using a higher-order (1,5) Padé approximant instead of the (1,3) approximant in (7) to arrive at the fifth-order model

$$U_T + (U^2)_X - \frac{\varepsilon^2}{6}U_{XXT} + \frac{7\varepsilon^4}{360}U_{XXXXT} = 0.$$

Similar models have been shown to admit such solutions.[6] While this is an interesting topic that pertains to admissibility of modulation shock solutions as mentioned earlier, we will not pursue the identification of such a heteroclinic orbit further herein.

4.4.2 | Modulation solution of the weakly nonlinear Whitham modulation equations

To obtain the form of an approximate modulation solution $\mathbf{q} = [\bar{u}, a, k]^T$ of the Whitham equations (31) that describes the TDSW, we appeal to the structure of the TDSW evident in Figure 11. An oscillatory wavetrain emerges from the left level u_- with increasing amplitude that saturates at a periodic traveling wave. The traveling wave then abruptly transitions to the right level u_+. Guided by previous work on the TDSW solutions of the KdV5 equation,[6] we make the self-similar modulation ansatz ($\xi = X/T = n/t$)

$$\mathbf{q}(\xi) = \begin{cases} \mathbf{q}_- & \xi < \lambda_2(\mathbf{q}_-), \\ \mathbf{q}_{\mathrm{RW}}(\xi) & \lambda_2(\mathbf{q}_-) \le \xi < \lambda_2(\mathbf{q}_\mathrm{p}), \\ \mathbf{q}_\mathrm{p} & \lambda_2(\mathbf{q}_\mathrm{p}) \le \xi < \lambda_2(\mathbf{q}_+), \\ \mathbf{q}_+ & \lambda_2(\mathbf{q}_+) \le \xi \end{cases} \tag{80}$$

for Equation (37) where λ_2 is the middle characteristic velocity. In addition, the constant states are

$$\mathbf{q}_- = [u_-, 0, k_-]^T, \quad \mathbf{q}_\mathrm{p} = [\overline{u}_\mathrm{p}, a_\mathrm{p}, k_\mathrm{p}]^T, \quad \mathbf{q}_+ = [u_+, a_+, 0]^T, \tag{81}$$

and $\mathbf{q}_{\mathrm{RW}}(\xi)$ is the rarefaction solution (integral curve) of Equation (39) for the second characteristic field $(\lambda_2, \mathbf{r}_2)$ that continuously connects the harmonic edge state $\mathbf{q}_-$ and the periodic traveling wave state $\mathbf{q}_{\mathrm{p}}$ of the TDSW. The discontinuity from $\mathbf{q}_{\mathrm{p}}$ to $\mathbf{q}_+$ satisfies the jump conditions (41) for the Whitham modulation equations where $V = \lambda_2(\mathbf{q}_+)$ is simultaneously the phase speed of the periodic traveling wave with parameters $\mathbf{q}_{\mathrm{p}}$, the shock speed, and the phase speed of the solitary wave with parameters $\mathbf{q}_+$, that is, it represents the TW component of the TDSW solution. The modulation solution (80) corresponds to a rarefaction-shock solution of the Whitham modulation equations.

The five parameters $(k_-, \mathbf{q}_{\mathrm{p}}, a_+)$ in the modulation solution (80) can, in principle, be obtained by solving the full Whitham modulation equations (31), but we lack explicit periodic traveling wave solutions to do so. Instead, we approximate the modulation solution (80) in the weakly nonlinear regime by solving Equations (48).

A general feature of Whitham modulation systems in the weakly nonlinear regime is the $\mathcal{O}(a^2)$ mean induced by the finite amplitude modulated wavetrain.[1] Absent mean changes due to initial/boundary data, the third-order weakly nonlinear modulation system (48) can be simplified, with the same order of accuracy, to a second-order modulation system. The procedure to do so is as follows. The induced mean is represented by the ansatz

$$\overline{u}(X,T) = u_0 + a(X,T)^2 u_2(k(X,T)) + \cdots, \tag{82}$$

where $u_0 \in \mathbb{R}$ is a constant background. This introduces the induced-mean coefficient $u_2(k)$ that gives rise to an effective nonlinear frequency shift $\tilde{\omega}_2$ by inserting (82) into Equation (43) and expanding as

$$\begin{aligned} \omega(k,\bar{u}) &= \omega_0(k,u_0) + a^2(\omega_2(k,u_0) + \partial_{\overline{u}}\omega_0(k,u_0)u_2(k)) + o(a^2), \\ &\equiv \omega_0(k,u_0) + a^2\tilde{\omega}_2(k,u_0) + o(a^2). \end{aligned} \tag{83}$$

With this effective nonlinear frequency shift, weakly nonlinear wave modulations are generically described by the simplified system[1]

$$\left(a^2\right)_t + \left(\omega_{0,k}a^2\right)_x = 0, \tag{84a}$$

$$k_t + (\omega_0)_x + \tilde{\omega}_2\left(a^2\right)_x = 0, \tag{84b}$$

provided

$$u_2(k) = -\frac{1}{16u_0(1-\cos k)}, \quad \tilde{\omega}_2(k) = \frac{(\cos k - 2)\cot(k/2)}{16u_0}. \tag{85}$$

Note that the additional coupling term involving $\tilde{\omega}_2$ and its derivatives contribute at higher order in a. The induced-mean coefficient $u_2(k)$ in Equation (85) is determined by compatibility of averaged mean, energy conservation laws (48a), (48b) with the induced-mean modulation system (84), which asymptotically satisfies $(F(k)a^2)_T + (F(k)\omega_{0,k}a^2)_X = 0$ for any differentiable F, in particular $F(k) = u_2(k)$.

Under the assumption of induced-mean variation, we can analytically obtain the rarefaction solution $\mathbf{q}_{\mathrm{RW}}(\xi)$ in (80) by solving Equation (84) for an RW and then inserting it into Equation (82).

For this, we express the induced-mean modulation system in Riemann invariant form

$$\frac{\partial r_\pm}{\partial t} + \lambda_\pm \frac{\partial r_\pm}{\partial x} = 0, \tag{86}$$

where

$$\begin{aligned} r_\pm &= a \mp \frac{1}{2} \int \left(\frac{\omega_{0,kk}}{\tilde{\omega}_2} \right)^{1/2} dk \\ &= a \mp 2\sqrt{2}\, u_0 \cos^{-1}\left(\frac{1}{3}(-1 + 2\cos k) \right), \quad u_0 > 0, \quad 0 < k < \pi, \quad a \geq 0. \end{aligned} \tag{87}$$

The restriction to positive mean and wavenumber is due to the fact that we have selected the positive square root in (87). The characteristic velocities are

$$\lambda_\pm = 2u_0 \cos k \pm \frac{a}{2} \cos\left(\frac{k}{2}\right) \sqrt{2 - \cos k}, \tag{88}$$

so that $\lambda_+ = \lambda_2$ and $\lambda_- = \lambda_1$ in Equation (50).

We can now solve for $\mathbf{q}_{\mathrm{RW}}(\xi)$ in (80) by setting $u_0 = u_-$ and taking the fast RW solution of Equation (86) that satisfies $r_- = \text{const}$ and $\lambda_+ = \xi$. The constant slow Riemann invariant r_- implies

$$\cos^{-1}\left(\frac{1}{3}(-1 + 2\cos k_-) \right) = \frac{a_\mathrm{p}}{4\sqrt{2}u_-} + \cos^{-1}\left(\frac{1}{3}(-1 + 2\cos k_\mathrm{p}) \right), \tag{89a}$$

and the assumption of induced mean implies

$$\overline{u}_\mathrm{p} = u_- + u_2(k_\mathrm{p}) a_\mathrm{p}^2. \tag{89b}$$

The RW profile is obtained by inverting $\lambda_+ = \xi$ for $a(\xi)$ and $k(\xi)$ subject to the constraint

$$\cos^{-1}\left(\frac{1}{3}(-1 + 2\cos k_-) \right) = \frac{a(\xi)}{4\sqrt{2}u_-} + \cos^{-1}\left(\frac{1}{3}(-1 + 2\cos k(\xi)) \right). \tag{89c}$$

Equations (89a) and (89b) are two conditions on the four unknown solution parameters $(k_-, \overline{u}_\mathrm{p}, a_\mathrm{p}, k_\mathrm{p})$. The other two conditions are obtained from the jump conditions (41).

The sharp transition from the periodic traveling wave $\mathbf{q}_\mathrm{p}$ to the solitary wave ahead $\mathbf{q}_+$ is achieved by a shock solution of the Whitham modulation equations. We obtain the jump conditions from the conservation laws (31a) and (31b) by assuming that the periodic traveling wave is in the weakly nonlinear regime (42) and the level ahead is a solitary wave where $k \to 0$, both with the same phase speed V:

$$-V(\overline{u}_\mathrm{p} - u_+) + \overline{u}_\mathrm{p}^2 + \frac{1}{8}a_\mathrm{p}^2 - u_+^2 = 0, \tag{89d}$$

$$-V\left(\frac{1}{3}\overline{u}_\mathrm{p}^3 + \frac{1}{8}\overline{u}_\mathrm{p} a_\mathrm{p}^2 - \frac{1}{3}u_+^3 \right) + \frac{1}{2}\overline{u}_\mathrm{p}^4 + \frac{1}{4}a_\mathrm{p}^2\left(\overline{u}_\mathrm{p}^2 \cos(k_\mathrm{p}) + \frac{1}{2}u_\mathrm{p}^2 \right) - \frac{1}{2}u_+^4 = 0. \tag{89e}$$

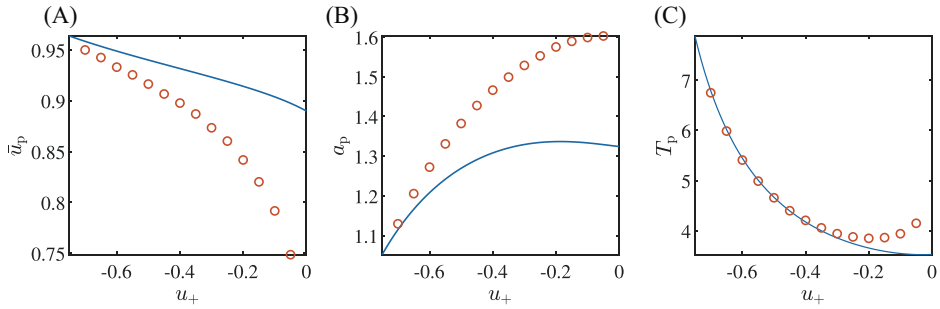

FIGURE 13 Traveling dispersive shock wave (DSW) parameters obtained from the modulation solution (80) (curves) and numerical simulation (circles).

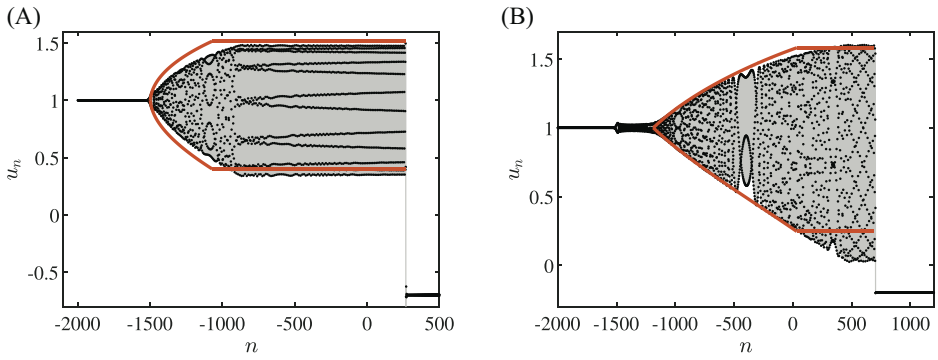

FIGURE 14 Two solutions at $t = 1000$ along with the envelope predictions from the modulation solution (80). (A) $u_+ = -0.7$ and (B) $u_+ = -0.2$.

The jump condition from the conservation of waves equation (31c) is satisfied because $\omega = k = 0$ for the solitary wave and $V = \omega_p/k_p$ for the periodic traveling wave

$$V = \frac{\omega_0(k_p, u_-) + a_p^2 \tilde{\omega}_2(k_p)}{k_p}. \tag{89f}$$

Solving for a_p and $\overline{u}_p$ from (89a) and (89b), then inserting them into (89d), (89e) and using the phase velocity (89f) determines two nonlinear equations for k_- and k_p. We solve these equations numerically using standard root finding methods to obtain all the parameters of the shock-rarefaction modulation solution (80) and compare it with numerical simulation in Figures 13 and 14. We observe in the figures that near the onset of the TDSW, the solution's mean, amplitude, and frequency are accurately captured by the above theory. On the other hand, as the amplitude of the solution increases, the approximation loses quantitative efficacy. Nevertheless, the qualitative trend of the solution's properties are captured by the above analysis.

With the parameters of the periodic solution available, we can then evaluate the characteristic velocities of the Whitham modulation equations in the weakly nonlinear limit, cf. Equations (48). These calculations show that the Whitham shock corresponding to the leading edge of the TDSW is refractive in the slowest characteristic family, weakly expansive in the middle characteristic family, and weakly compressive in the fastest characteristic family. Since the shock does not

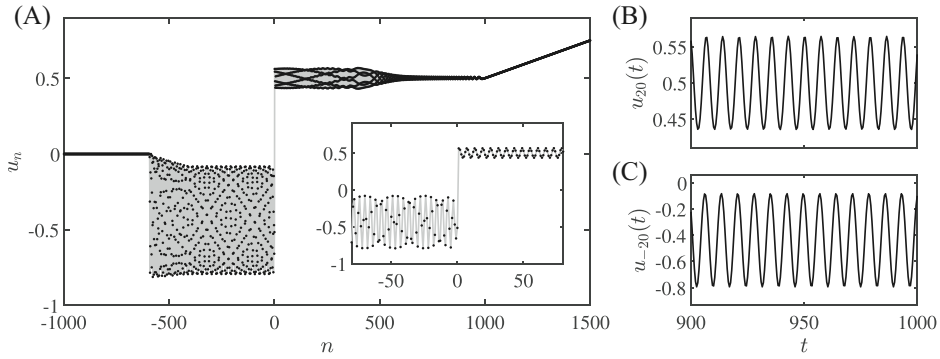

FIGURE 15 (A) Unsteady shock solution arising from step initial data (4) with $u_- = 0$ and $u_+ = 1$. (B, C) Series data of the evolution of lattice sites $n = +20$ (B) and $n = -20$ (C) for $t \in [900, 1000]$.

satisfy the classical Lax entropy conditions, it is nonclassical. Therefore, its admissibility requires further analysis. For example, one may be able to identify admissibility by identifying a heteroclininc solution of the discrete conservation law—analogous to the continuous case studied in Ref. 6.

4.5 | Unsteady shock

In Section 4.3, we found that for $u_+ = 1$ and $u_- \in (-1, -0.26)$, an SS separated two counterpropagating waves, one a DSW, the other an RW. When $u_- = -0.26$, the DSW no longer separates from the SS. Instead, the DSW + SS + RW is numerically observed to bifurcate into the unsteady generation of counterpropagating periodic waves that we term an US for $u_- \in (-0.26, 0.18)$. When u_- exceeds 0.18, the US bifurcates into an RW, described in Section 4.1. We now investigate the US.

A plot of the solution for $u_- = 0$ and $u_+ = 1$ is given in Figure 15. Two distinct counterpropagating periodic waves traveling with speed $c_\pm$ emerge from the origin that then transition to the constant level u_- behind through a partial DSW and to u_+ ahead via a partial DSW and an RW. While the velocities $c_\pm$ are distinct, Figure 15B depicting the time series $u_{\pm 20}(t)$ indicates that the two periodic waves have approximately the same temporal frequency, which we confirm below numerically to high precision.

4.5.1 | Poincaré description

A spatiotemporal intensity plot of the US with $u_- = -0.16$ near $n = 0$ is shown in Figure 16A. The counterpropagating traveling waves can clearly be identified. While the underlying wave parameters of the left- and right-moving waves will generally be different, they do share the same frequency. Thus, the dynamics correspond to a time-periodic solution. Indeed, inspection of Figure 16C confirms this, which shows the same intensity plot as panel A, but with the solution sampled every T time units, where T is the period of oscillation. This is the Poincaré map of the dynamics. With this sampling size, the solution appears to be constant, suggesting that the waveform is genuinely time-periodic. To demonstrate this further, we simulated the equations of motion on a small lattice $n \in [-20, 20]$ with boundary conditions given by the periodic solution, that is, the left boundary is given by $u_{-20}(t)$ and the right boundary is given by $u_{20}(t)$. The

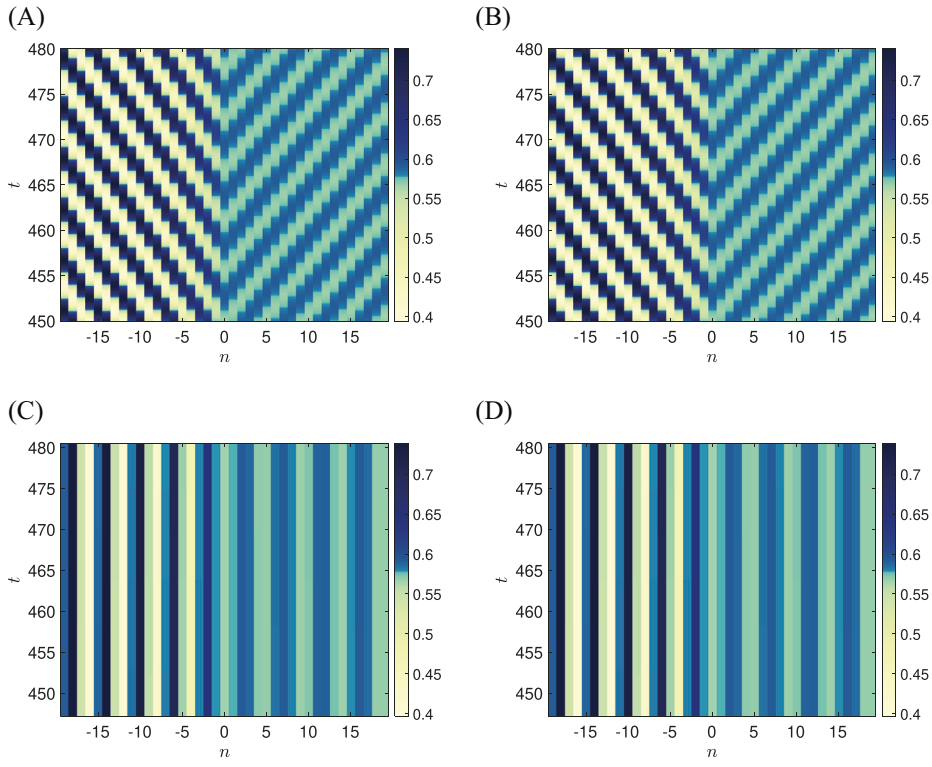

FIGURE 16 Intensity plot of the absolute value of the displacement with $u_- = 0.16$ and $u_+ = 1$ for the full simulation (aA) and truncated simulation (B) for $n = -20 \ldots 20$ with forced boundaries. Panels (C) and (D) show the Poincaré map of the solution in (A) and (B), respectively, evaluated at every period.

dynamics upon initialization with the periodic solution $u_n(450)$ are shown in Figure 16B, which can be hardly distinguished from the dynamics in (A). The evolution remains periodic, as can be inferred from Figure 16D, which are the dynamics sampled every T seconds. An avenue for potential further study, prompted by these findings, is the seeking of exact time-periodic solutions of the model and their corresponding Floquet analysis.

4.5.2 | Approximation of traveling waves via quasi-continuum model

If considering the left- and right-moving waves as separate entities, we can once again apply the quasi-continuum reduction to describe the traveling wave using Equation (79). A comparison of the spatial profile of the left-moving wave with $u_+ = -0.16$ at time $t = 480$ is shown in Figure 17A. The phase plane for the left-moving waves (left lobes) and right-moving waves (right lobes) is shown in Figure 17B in markers, with corresponding quasi-continuum approximations shown as solid lines. Like before, the reduction is best for smaller step heights (compare the blue and red orbits in panel B). A comparison of the mean, amplitude, and frequency of the simulation and quasi-continuum approximation as a function of u_- is shown in panel C for both the left- and right-moving waves. We can observe that the approximation provides a very adequate description of the relevant traveling patterns.

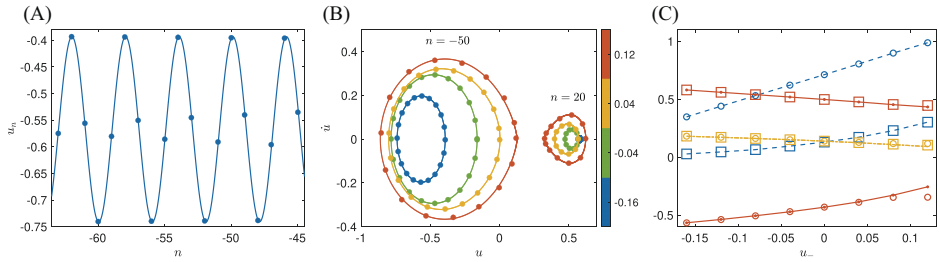

FIGURE 17 (A) Zoom of the left periodic wave with $u_- = -0.16$ (blue markers) and quasi-continuum approximation (solid blue line). (B) Plot of the phase plane $(u_{-50}(t), \dot{u}_{-50}(t))$ (left lobes) and $(u_{20}(t), \dot{u}_{20}(t))$ (right lobes) for a time interval such that the periodic wave has developed. The color intensity corresponds to the value of u_-. In particular, $u_- = -0.16$ (blue), $u_- = -0.04$ (green), $u_- = 0.04$ (yellow), $u_- = 0.12$ (red). The solid markers are the corresponding quasi-continuum approximations. (C) Plot of the mean (red solid lines), amplitude (blue dashed lines), and frequency $1/T$ (yellow dashed-dot line) as a function of u_-. The quasi-continuum approximation of these wave parameters is shown as open circles (for the left wave, $n = -50$) and open squares (for the right wave, $n = 20$).

4.5.3 | Jump conditions

Figure 16 shows two counterpropagating periodic traveling waves with a rapid transition between them in the vicinity of $n = 0$. This motivates the hypothesis that these two waves satisfy the jump conditions obtained from the Whitham modulation system's conservation laws. We denote the periodic traveling waves by $\varphi_\pm$ for the left $(-)$ and right $(+)$ periodic waves, respectively. For a discontinuous shock solution of the Whitham system at the origin, the corresponding jump conditions are Equation (41):

$$\left\langle \Phi'(\varphi_-) \right\rangle - \left\langle \Phi'(\varphi_+) \right\rangle = 0, \tag{90a}$$

$$\left\langle \Phi'(\varphi_-) \mathcal{S}\Phi'(\varphi_-) \right\rangle - \left\langle \Phi'(\varphi_+) \mathcal{S}\Phi'(\varphi_+) \right\rangle = 0, \tag{90b}$$

$$\omega_- - \omega_+ = 0, \tag{90c}$$

where $\mathcal{S}$ is the unit shift operator $\mathcal{S}R(\eta) = R(\eta + 1)$, and $\square$ is defined as in Eq. (71). To check if these jump conditions are indeed satisfied, we approximate the above averages using the numerical simulations. In particular, we let the structure come close to a periodic state (as in Figure 16) and extract one period of motion at a particular node n. Let T_n be the period of node n and let $I_{T_n} = [\tau, \tau + T_n]$ be the corresponding time interval from $t = \tau$. We then make the following approximations:

$$\left\langle \Phi'(\varphi) \right\rangle \approx \frac{1}{T_n} \int_{I_{T_n}} \Phi'(u_n(t)) dt =: f(n), \tag{91a}$$

$$\left\langle \Phi'(\varphi_-) \mathcal{S}\Phi'(\varphi_-) \right\rangle \approx \frac{1}{T_n} \int_{I_{T_n}} \Phi'(u_n(t)) \Phi'(u_{n+1}(t)) dt =: g(n) \tag{91b}$$

for $\tau \gg 1$ (we set $\tau = 240$ in what follows). The first jump condition, Equation (90a), is checked by comparing $f(-5)$ to $f(5)$, while the second jump condition Equation (90b) is checked by

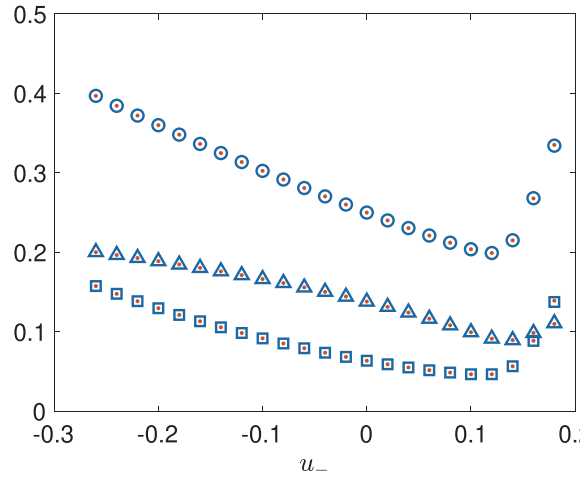

FIGURE 18 Numerical verification of the jump conditions (90) of the Whitham equations as u_- is varied for the US solution. Open blue circles: $\langle \Phi'(\varphi_-)|_{n=-5}\rangle \approx f(-5)$. Open blue squares $\langle \Phi'(\varphi_-)S\Phi'(\varphi_-)\rangle|_{n=-5} \approx g(-5)$. Open blue triangles: $\omega_-|_{n=-5} \approx 1/T_{-5}$. Red dots: corresponding quantities evaluated at $n = +5$. Because the red dots lie inside the open blue markers, the jump conditions are satisfied to high accuracy.

comparing $g(-5)$ with $g(5)$. The third jump condition is simply the difference in the frequency, which we estimate via $1/T_{-5}$ and $1/T_5$. Figure 18 shows a plot of $f(-5)$ (open blue circles), $g(-5)$ (open blue squares), and $1/T_{-5}$ (open blue triangles), while the red dots show the corresponding quantities for $n = 5$. Notice that each red point falls nicely into an open blue marker, indicating that the jump conditions are, up to some small numerical error, satisfied. The maximum residual over the interval of u_- values tested for the first jump condition was $\max_{u_+} |f(-5) - f(5)| \approx 0.001$, whereas the maximum residual for the second condition was 0.0017 and the maximum residual for the third was 0.0008.

The numerical evidence is a compelling indication that the US can be interpreted as a shock solution of the Whitham modulation equations. While shock solutions of the Whitham equations have been constructed previously,[6,50] the previous definition of admissibility requires the existence of traveling wave solutions of the corresponding continuum PDE in which the phase velocities and shock velocity all coincide. In the present case of the US for the lattice equation (3), all three of these velocities differ but the frequencies are the same. This suggests a new class of admissible shock solutions to the Whitham equations corresponding to time-periodic solutions of the lattice equation, an intriguing possibility for future work.

We also note the similarity between the US and defect solutions of reaction–diffusion equations.[54] Because the waves in the US are in-phase (see Figure 16), it most closely resembles a target pattern with a source from which waves are emanating, in the language of Ref. 54. The target pattern exhibits a Hopf bifurcation of the background state and a specific transition of the eigenvalues associated with the linearized operator about the background state. It would be interesting to explore potential connections between the underlying diffusive regularization of the target pattern and the dispersive regularization of the US studied here.

4.6 | Blowup

In Section 4.4, we observed that a TDSW (a partial DSW connected to a traveling wave) is generated that transitions from the left level $u_- = 1$ to the right level $u_+ \in (-0.724, 0)$. By decreasing the value of u_+ below -0.724, a new wavetrain develops on the right level. Figure 19 shows three example profiles. When u_+ is close to the transition value $u_+ = -0.724$, the excitation on top of the right level u_+ is small (see Figure 19A). Decreasing u_+ further results in a larger amplitude

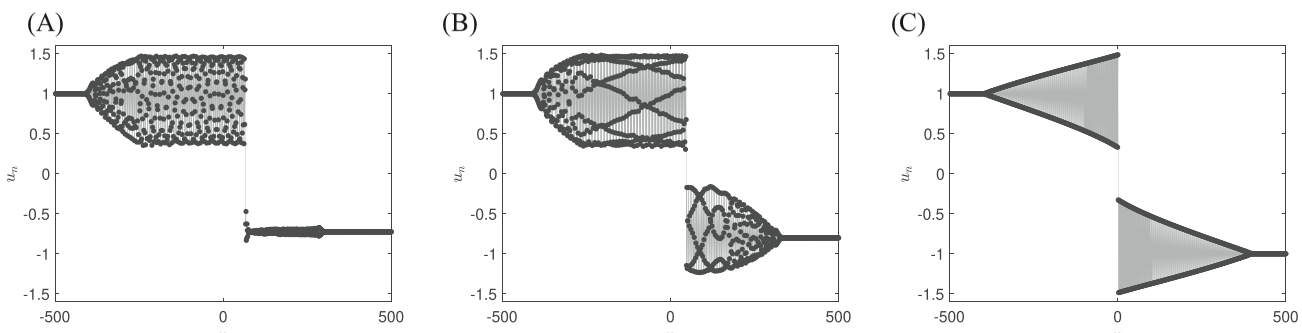

FIGURE 19 Snapshots of the spatial profile at $t = 200$ for (A) $u_+ = -0.725$, (B) $u_+ = -0.8$, and (C) $u_+ = -0.999$.

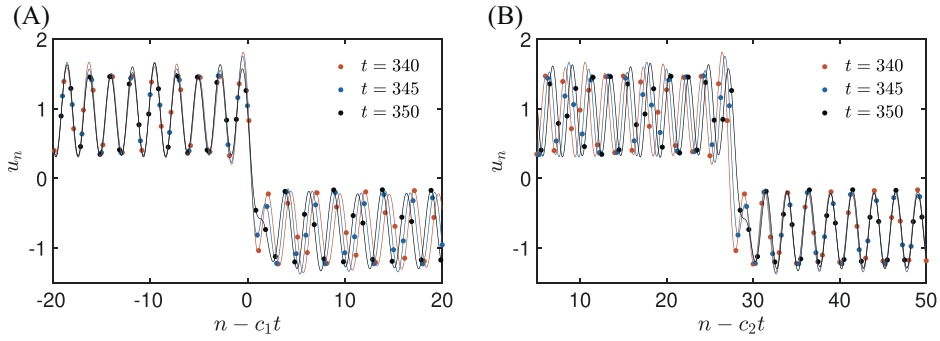

FIGURE 20 Interpolated spatial profiles at different times in the comoving frame for $u_+ = -0.8$ with speed (A) $c_1 = 0.229$, (B) $c_2 = 0.15$ demonstrating that the waves to the left and right of the sharp transition move at different speeds.

wavetrain that resembles another TDSW (see Figure 19B). Close to $u_+ = -1$, the wavetrains on the left and right levels approach binary oscillations, as shown in Figure 19C. Solution dynamics similar to those shown in Figure 19C, but with odd initial data, were studied extensively in Ref. 16. In the work of Turner and Rosales,[16] it is claimed that the emergence of blowup for the odd initial data they considered is "almost always" associated with the emergence of regions of binary oscillations for which the upper and lower oscillatory envelopes have opposite sign. Such a scenario was observed to result in the loss of hyperbolicity in the modulation equations (10) for binary oscillations and, consequently, a dynamical instability and thus exponential growth in a localized region of space that ultimately led to the finite-time blowup of the wave pattern. It was also shown that the wave pattern near the blowup closely resembles a self-similar solution of the lattice equation, $u_n = a_1(n + a_3)/(t + a_3)$ with a_1, a_2, a_3 being appropriate constants (see Ref. 16 for details).

For the Riemann data considered here (4), we numerically observe blowup in regions of the solution where binary oscillations are not apparent, which we now explore.

We will start with a more detailed discussion of the structure in Figure 19B with $u_+ = -0.8$, which is representative of many of the patterns found for $u_+ \in (-1, -0.724)$ and $u_- = 1$. A zoom-in of the solution in the comoving frame $n - ct$ near the shock interface is shown in Figure 20 at three separate times ($t \in \{340, 345, 350\}$) represented by different colors. Both the solution on the lattice (dots) and its zero-padded Fourier interpolant (curves) are shown with two different speeds. In Figure 20A with speed $c = c_1 = 0.229$, the leftmost wave at the three distinct times overlap, suggesting that it moves in the steady frame $n - c_1 t$. Contrastingly, in Figure 20B with speed $c = c_2 = 0.15$, the rightmost wave at the three distinct times overlap, suggesting it moves in the slower steady frame $n - c_2 t$. The spatial profile at $t = 350$ and the Fourier transform $\hat{u}(k)$ of a 40-site window of the leftmost (rightmost) wave are shown in Figure 21A in red (blue). Each wave has wavenumber concentration, and they are distinct ($k \approx 2.76$ for the left and $k = 2.51$ for the right). This solution is a generalization of the US studied in Section 4.5 in that two traveling waves are connected through a sudden jump. However, there are key differences. First, the shock interface itself is moving as shown in Figure 20. Second, the frequency for the leftmost and rightmost waves are not identical, which can be seen in Figure 21C that shows the time series at a node located at the left wave ($n = 20$) and the right wave ($n = 250$). Here, it is clear that the oscillation frequencies are distinct. We conjecture that, much like the US, this wavetrain can be modeled by a discontinuous, weak solution of the Whitham equations satisfying the jump conditions (41).

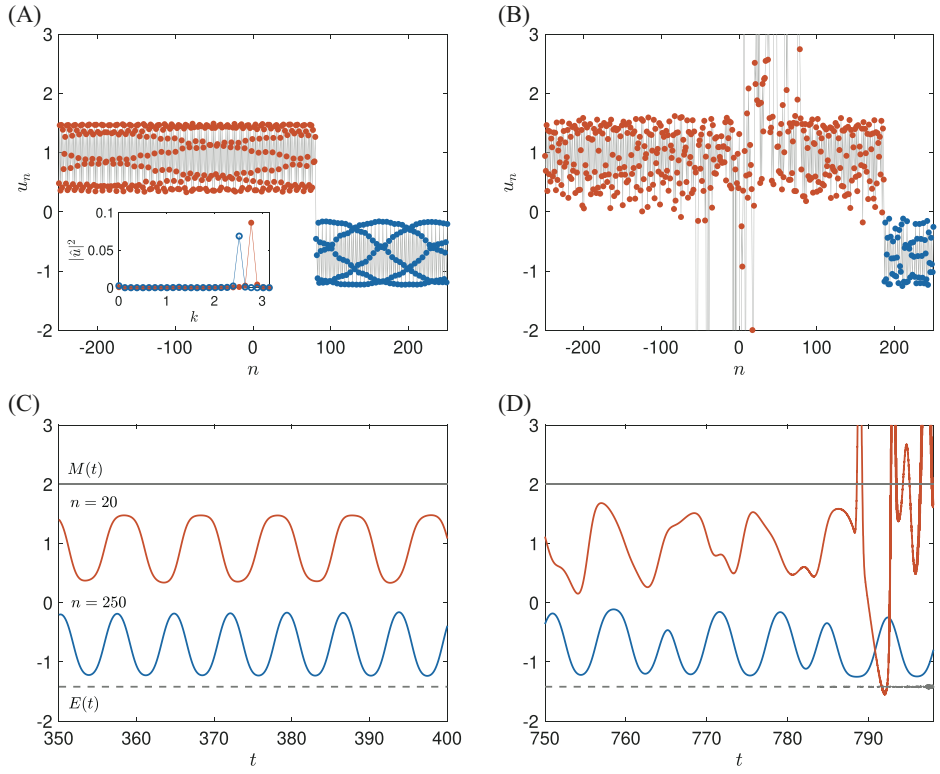

FIGURE 21 Various zooms of the solution with $u_- = 1$ and $u_+ = -0.8$. (A) Zoom of spatial profile near the interface with $t = 350$. The inset shows the spatial Fourier transform of the left wave (red) and right wave (blue). (B) Zoom of spatial profile near the interface with $t = 800$, very close to the blowup time. (C) Time series of the $n = 20$ node (red) and $n = 250$ node (blue) much before the blowup. The mass $M(t)$ is shown as the solid gray line, and the energy $E(t)$ is also shown as a dashed gray line. Note that both are vertically displaced for visual purposes. The actual values are $E(0) = 0.0813$ and $M(0) = 0.1$. (D) Same as (C), but for a time interval closer to the blowup time.

Rather than pursue this further, we instead turn to an examination of the large t dynamics of the solution and, specifically, its eventual blowup.

This structure is relatively coherent until about $t = 600$, after which small disturbances in the leftmost wave develop. Disturbances are noticeable if one compares the time series for $t \in (350, 400)$ (shown in Figure 21C) and for $t \in (750, 800)$ (shown in Figure 21D). At about $t = 816$, the solution appears to experience finite-time blowup. Figure 22A shows the blowup. The spatial profile close to (but before) the time of blowup is shown in Figure 21B. Notice that the location of the blowup is spatially concentrated within the leftmost wave and that the wavenumber of the traveling wave where the instability seems to manifest is about $k \approx 2.76$, (i.e., not a binary oscillation).

We conjecture that the observed blowup is due to an instability of the leftmost wave with wavenumber $k \approx 2.76$, and not due to numerical instability. A piece of evidence in this direction is that the mass and energy are conserved until times very close to the blowup time. The solid gray and dashed lines of Figure 21C,D show the mass $M(t)$ and energy $E(t)$, respectively. Note that in order for these quantities to be conserved, we employ periodic boundary conditions. For the simulations in this subsection, we concatenate the initial condition equation (4) with its

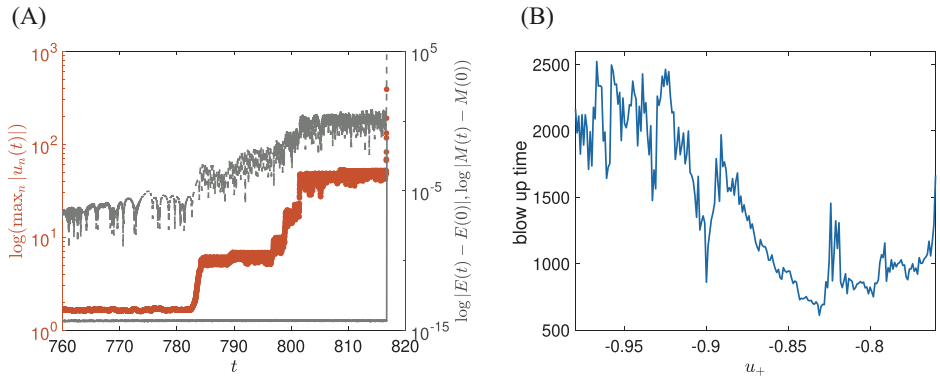

FIGURE 22 (A) Semilog plot of $\max_n |u_n(t)|$ versus time leading to blowup (red). The semilog plot of $|E(t) - E(0)|$ (dashed gray line) and $|M(t) - M(0)|$ (solid gray line) are also shown. (B) Observed blow-up time for various values of u_+ with $u_- = 1$ fixed. The lattice size is $2N = 100000$ and we simulate until $t = 10000$. For $u_- \geq -0.725$, we observed no blowup.

reflection about the first site, leaving us with $2N$ total nodes. Thus, the relevant window of space for the plots is only the second half of the lattice. We define the lattice indices so that the initial ($t = 0$) jump from u_- down to u_+ occurs at $n = 0$. This makes the plots consistent with those in the previous sections. We include the entire spatial window for the computation of $E(t)$ and $M(t)$. Note that in Figure 21C,D the quantities $M(t)$ and $E(t)$ are indeed conserved, even as the waveform begins to break down (see $t \approx 790$ of panel, Figure 21D). The gray solid and dashed lines of Figure 22A show plots of $M(t)$ and $E(t)$, respectively, for times leading to the blowup itself. While the energy $E(t)$ remains constant after the strong onset of instability at about $t = 785$, the energy conservation breaks down for $t > 800$, while $M(t)$ remains conserved. The conservation of mass in the numerical scheme is not surprising, since by direct computation one sees that the variational integrator applied to Equation (35) with $\Phi'(u) = u^2$ conserves the mass exactly.[32] The near conservation of energy for the variational integrator relies on the boundedness of the underlying numerical solution.[55] This will be clearly violated for solutions exhibiting collapse-type phenomena and thus it is not surprising that the energy is not conserved in the numerical scheme close to the time of blowup. Thus, it seems the initial collapse is due to instability of the wave (energy remains conserved for $t < 790$), but after experiencing sustained large amplitude oscillations, the numerical scheme may begin to exhibit additional numerical instabilities (since energy is not conserved for $t > 790$). The blowup time found here is an approximation that depends on the particulars of the numerical scheme.

For $u_+ \in (-1, -0.724)$ and $u_- = 1$, we observe a similar blowup of the solutions, with the blowup time varying roughly between $t = 700$ and $t = 2500$ (see Figure 22B). We define the solution as blown-up once $\max_n |u_n|$ exceeds a large threshold. We practically used 1000 as the threshold (the actual threshold makes little difference in Figure 22B since the blowup occurs so quickly). For this figure panel, we used a lattice size of $2N = 100000$ and simulated until $t = 10000$. We observe blowup with $u_+ = -0.725$ (at about $t = 1500$) but no blowup with $u_+ = -0.724$, even when simulating until $t = 10000$. This sharp transition between finite-time blowup and no blowup is further evidence that the blowup is due to an underlying instability of the waveform and not due to numerical instability.

The question of stability of traveling waves of this lattice is thus an important open question, meriting further investigation. Based on these findings, it appears that traveling waves with

wavenumbers other than $k = \pi$ can lead to instabilities and finite-time blowup, a generalization of the findings in Ref. 16 where binary oscillations with $k = \pi$ were identified as a primary instability mechanism.

5 | NONUNIQUENESS OF RIEMANN PROBLEMS

As already mentioned in the introduction, the solutions to the Whitham system (31) are nonunique for certain classes of initial data. To discuss this in greater detail, we start with some preliminary comments concerning the inviscid Burgers' PDE (1), which describes the dispersionless, hyperbolic scaling limit of the lattice (3) in the case of no oscillations and is a subsystem of (31) that governs the dynamics in the case of zero wave amplitude or zero wavenumber. To obtain an elementary example for nonuniqueness, we impose the odd initial condition

$$u(x,0) = \operatorname{sign}(x) \tag{92}$$

and notice that the RW

$$u(x,t) = U(x/t) \qquad \text{with} \qquad U(\xi) = \begin{cases} -1 & \text{for} \quad -\infty < \xi < -2 \\ \xi/2 & \text{for} \quad -2 < \xi < +2 \\ +1 & \text{for} \quad +2 < \xi < +\infty \end{cases} \tag{93}$$

is the unique self-similar solution according to the classical theory of hyperbolic conservation laws (see, for instance, Ref. 2). The latter complements the PDE with an additional selection rule to exclude solutions that are considered to be unphysical. The most prominent example is the Lax condition for shocks, but without such an admissibility criterion there exists a plethora of possibilities to fulfill the initial-value problem (1)+(92). For instance, the formulas

$$U(\xi) = \begin{cases} -1 & \text{for} \quad -\infty < \xi < -2 \\ \xi/2 & \text{for} \quad -2 < \xi < -2\,\mu \\ -\mu & \text{for} \quad -2\,\mu < \xi < 0 \\ +\mu & \text{for} \quad 0 < \xi < +2\,\mu \\ \xi/2 & \text{for} \quad +2\,\mu < \xi < +2 \\ +1 & \text{for} \quad +2 < \xi < +\infty \end{cases} \qquad \text{and} \qquad U(\xi) = \begin{cases} -1 & \text{for} \quad -\infty < \xi < -1-\mu \\ -\mu & \text{for} \quad -1-\mu < \xi < 0 \\ +\mu & \text{for} \quad 0 < \xi < +\mu+1 \\ +1 & \text{for} \quad +\mu+1 < +\infty \end{cases} \tag{94}$$

provide two families of further self-similar solutions in dependence of the real parameter $0 < \mu < 1$ and $\mu > 1$, respectively, and contain (93) as limiting case for $\mu = 0$. The corresponding profile functions U are illustrated in Figure 23 and combine a steady discontinuity at $x = 0$ (which violates the Lax condition on both sides) with either two RWs or two Lax shocks. In numerical simulations of the lattice (3), we find a related family of solutions that differ only in microscopic details of the imposed initial conditions. As a typical but still elementary example we study the lattice initial data

$$u_n(0) = \begin{cases} -1 & \text{for} \quad n < 0 \\ \eta & \text{for} \quad n = 0 \\ +1 & \text{for} \quad n > 0, \end{cases} \tag{95}$$

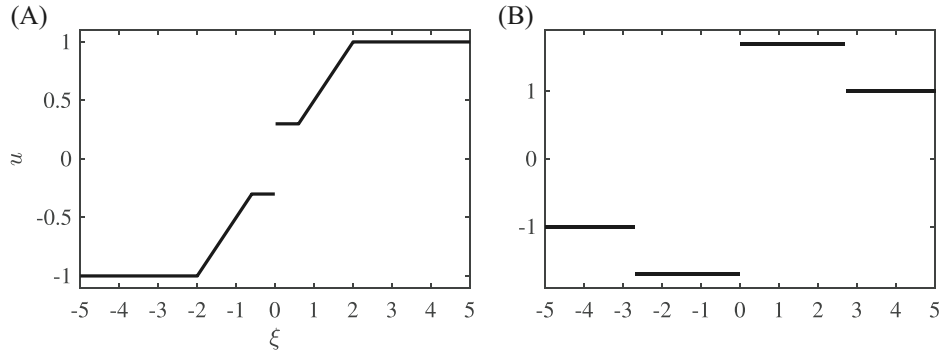

FIGURE 23 Solutions from (94) with (A) $\mu = 0.3$ and (B) $\mu = 1.7$ to the inviscid Burgers' equation (1) with initial data (92).

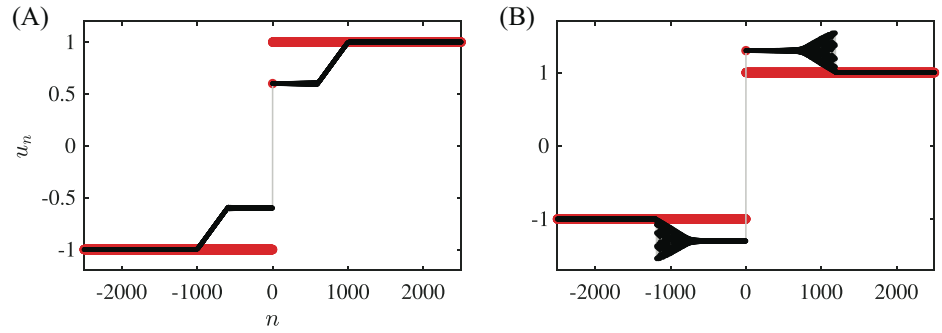

FIGURE 24 Lattice solution with initial data (95) and two choices of the microscopic parameter (A) $\eta = 0.5$ and (B) $\eta = 1.3$ at $t = 500$. The initial data are shown in red.

where the free parameter η reflects that the macroscopic Riemann data (92) can be realized in many different ways on the microscopic scale. Figure 24 reveals that the numerical solutions for different choices of η correspond to distinct waves on the macroscopic scale. We always find a steady discontinuity at $x = 0$ but its jump height as well as the other waves depend crucially on the value of microscopic parameter. In analogy to Figure 23, we observe two RWs in the case of $0 < \eta < 1$ but for $\eta > 1$ we have to replace the Lax shocks by DSWs.

It remains a challenging task to understand the macroscopic impact of small-scale fluctuations in the initial data. For instance, it seems that the parameter η in (95) determines the jump height of the emerging steady discontinuity in Figure 24 but we are not aware of any heuristic or even rigorous explanation thereof. Numerical simulations also indicate that microscopic details might not be relevant for Riemann data that are either positive or negative on both sides but also this must be investigated more thoroughly. Both issues are also intimately related to the properties of the Whitham system (33) which can be regarded as an extension of the Burgers' equation (1). At least for sign changing Riemann problems, the lattice (3) is able to produce an entire family of Whitham solutions and it is very natural to investigate and classify them in terms of selection criteria and entropy inequalities. Moreover, other nonlinearities might produce further effects due to linearly degenerated states in the scalar first-order PDE corresponding to (12); see Refs. 47, 56 for a related problem in FPUT chains whose force functions are increasing with inflection point.

6 | CONCLUSIONS AND FUTURE CHALLENGES

In the present work, we revisit the first-order nonlinear dynamical lattice of Equation (12) through the lens of "lattice hydrodynamics" by providing a systematic analysis of the solutions to the canonical lattice Riemann problem (4) for the case of quadratic flux (3). Building on earlier works of Refs. 16, 30, 32, we have characterized DSWs and RWs, familiar from continuum dispersive hydrodynamics. But we also discover a variety of nonclassical hydrodynamic-like solutions. In addition to finite-time blowup, recognized earlier in the work of Turner and Rosales,[16] we identify three additional dynamical regimes that are interpreted using a combination of numerical simulation, quasi-continuum approximation, and Whitham modulation theory. These regimes include the generation of a counterpropagating DSW and RW pair separated by a stationary, abrupt shock. In addition, an abrupt, unsteady transition between two counterpropagating periodic waves with the same frequency is interpreted as a shock solution of the Whitham modulation equations. Finally, the phase diagram 1 of solutions to the lattice Riemann problem is rounded out by a TDSW, consisting of an unsteady partial DSW, connected to a heteroclinic periodic-to-equilibrium traveling wave.

These elements of the lattice model's phenomenology provide an opportunity to develop different aspects of the mathematical analysis of lattice hydrodynamics. For instance, we adapt the DSW fitting method of Ref. 49 to lattice equations in order to characterize the expansion and edge properties of lattice DSWs. We also follow up the work of Ref. 30, providing abstract modulation equations for a quasi-continuum analog of the lattice dynamical system. We connect these to the genuinely discrete modulation equations, made explicit in the weakly nonlinear regime by a Poincaré–Lindstedt expansion of periodic traveling wave solution profiles and their frequencies. Hyperbolicity and self-similar solutions of the modulation equations are used to characterize lattice hydrodynamics. The quasi-continuum theory was also leveraged elsewhere, such as in characterizing the leading edge amplitude of the DSW and the periodic/traveling wave solutions of the discrete model. A truncation of the dynamics in wavenumber space allows for a linearized, large t analysis of small amplitude oscillations that accompany the RW and DSW solutions.

Beyond the binary oscillations that have been studied previously, this work has identified new lattice hydrodynamic features that, so far, appear not to have a continuum, dispersive hydrodynamic parallel. Of particular interest is the rapid, unsteady transition between two in-phase counterpropagating periodic traveling waves with the same frequency (US in Figure 1), identified with a shock solution of the Whitham modulation equations. This solution is born out of the bifurcation of another lattice solution particular to the lattice, the counterpropagating DSW, RW pair separated by an SS (DSW + SS + RW in Figure 1) when the DSW merges with the SS. The US represents an unsteady generalization of the steady periodic-to-equilibrium heteroclinic solutions of higher-order continuum dispersive equations, themselves interpreted as admissible shock solutions of the corresponding Whitham modulation equations.[6,50] This work points to a new class of admissible "Whitham shocks" in the lattice context, though it remains to be seen what specific admissibility criteria, or entropy inequalities, are required for such solutions to exist. It will be interesting to see if continuum solutions of this type also exist.

The asymptotic and semianalytical tools used in this work constitute an effective framework in which to investigate the hydrodynamics of other lattice dynamical systems for which DSW phenomena may arise. For example, the Riemann problem for FPUT chains generalizes to two wave families (second order in time); the problem of a single wave family studied here has been shown to exhibit a variety of lattice hydrodynamic solutions, including steady transition fronts[57] and DSWs.[58]

A number of interesting open questions remain. Here, we list some of these. While the existence of periodic traveling waves has been proven,[32] their stability and the existence, as well as stability of a more general class of traveling waves consisting of periodic-to-periodic heteroclinic solutions are important problems to better understand lattice hydrodynamics, with implications for finite-time blowup and the construction of the TDSW solution. In the DSW + SS + RW solution, we have not been able to provide a mechanism that leads to the particular selection of the intermediate constant $u_0 = (u_+ - u_-)/2$. We suspect that this is due to microscopic details of the lattice equation that have been neglected in the analysis. Of similarly unknown origin is the selection mechanism for shock solutions of the binary modulation equations (10) investigated in detail in Ref. 16. On the other hand, the US constitutes a genuine time-periodic orbit. Such periodic orbits are worthy of exploration in their own right, including from the perspective of dynamical systems by, for example, generalizing the spatial dynamics in dispersive[50] and dissipative[54] systems. The existence, stability, and bifurcation analysis of such states are intriguing problems for future exploration that portend an admissibility criterion for a class of modulation shock solutions. Such an admissibility criterion would be physically meaningful. Yet another interesting research direction to pursue is the identification of equivalent admissibility criteria that are easier to apply. Whether a suitable entropy function and entropy inequality can be identified to determine admissibility of modulation shocks remains an interesting open question for further study. As discussed in Ref. 16, the model with quadratic flux (3) analyzed herein is one among several possible discretizations of the inviscid Burgers' equation. A comparative study of different discretizations of the more general conservation law $u_t + \Phi'(u)_x = 0$ could lead to other lattice hydrodynamics and, in the case of integrable discretizations, be amenable to deeper mathematical analysis. These topics constitute some of the open problems within the theme of DSWs in one spatial dimension. The study of higher-dimensional models appears to be wide open. Some of these topics are currently under consideration and will be reported in future publications.

ACKNOWLEDGMENTS

One of our coauthors, Michael Herrmann, tragically passed away while this paper was still under review. Those who had the privilege of working with Michael know that his contributions and insights were truly invaluable. Over the years spent on this project, each of us learned immensely from him. We witnessed firsthand that he was not only a world-class mathematician but also a generous, kind, and joyful individual. Michael, our esteemed collaborator and dear friend, will be missed.

The authors would like to thank the Isaac Newton Institute for Mathematical Sciences for support and hospitality during the programme Dispersive Hydrodynamics when work on this paper was undertaken (EPSRC Grant Number EP/R014604/1). This material is also based upon work supported by the US National Science Foundation under Grants DMS-2107945 (C.C. and E.O.), DMS-2204702 (P.G.K.), PHY-2110030 (P.G.K), and DMS-2306319 (M.A.H.). This work began during P.S.'s time as INI-Simons Postdoctoral Research Fellow, and this author would like to thank the INI for support and hospitality during this fellowship, which was supported by Simons Foundation (Award ID 316017).

DATA AVAILABILITY STATEMENT

The data that support the findings of this study are available from the corresponding author upon reasonable request.

ORCID

Patrick Sprenger https://orcid.org/0000-0001-6654-8974
Christopher Chong https://orcid.org/0000-0003-1655-3382
P. G. Kevrekidis https://orcid.org/0000-0002-7714-3689
Mark A. Hoefer https://orcid.org/0000-0001-5883-6562

REFERENCES

1. Whitham GB. *Linear and Nonlinear Waves*. Wiley; 1974.
2. LeFloch PG. *Hyperbolic Systems of Conservation Laws: The Theory of Classical and Nonclassical Shock Waves*. Lectures in Mathematics, ETH Zürich. Birkhäuser Verlag; 2002.
3. Lax PD, Levermore CD. The small dispersion limit of the Korteweg-de Vries equation: 1–3. *Commun Pure Appl Math*. 1983;36(3,5,6):253-290;571-593;809-830.
4. Gurevich AV, Pitaevskii LP. Nonstationary structure of a collisionless shock wave. *J Exp Theor Phys*. 1973;65:590-604.
5. El GA, Hoefer MA. Dispersive shock waves and modulation theory. *Physica D*. 2016;333:11-65.
6. Sprenger P, Hoefer MA. Discontinuous shock solutions of the whitham modulation equations as zero dispersion limits of traveling waves. *Nonlinearity*. 2020;33(7):3268-3302.
7. Congy T, El GA, Hoefer MA, Shearer M. Dispersive Riemann problems for the Benjamin–Bona–Mahony equation. *Stud Appl Math*. 2021;147(3):1089-1145.
8. Hou TY, Lax PD. Dispersive approximations in fluid dynamics. *Commun Pure Appl Math*. 1991;44(1):1-40.
9. Ehrnström M, Groves MD, Wahlén E. On the existence and stability of solitary-wave solutions to a class of evolution equations of Whitham type. *Nonlinearity*. 2012;25(10):2903-2936.
10. Hur VY, Johnson MA. Modulational instability in the Whitham equation with surface tension and vorticity. *Nonlinear Anal Thoery Methods Appl*. 2015;129:104-118.
11. Binswanger AL, Hoefer MA, Boaz I, Sprenger P. Whitham modulation theory for generalized Whitham equations and a general criterion for modulational instability. *Stud Appl Math*. 2021;147(2):724-751.
12. Benjamin TB, Bona JL, Mahony JJ. Model equations for long waves in nonlinear dispersive systems. *Philos Trans R Soc Lond A*. 1972;272(1220):47-78.
13. Rosenau P. Hamiltonian dynamics of dense chains and lattices: or how to correct the continuum. *Phys Lett A*. 2003;311:39-52.
14. Rosenau P. Dynamics of nonlinear mass-spring chains near the continuum limit. *Phys Lett A*. 1986;118:222-227.
15. Nesterenko VF. *Dynamics of Heterogeneous Materials*. Springer-Verlag; 2001.
16. Turner CV, Rosales RR. The small dispersion limit for a nonlinear semidiscrete system of equations. *Stud Appl Math*. 1997;99:205-254.
17. El GA, Hoefer MA, Shearer M. Dispersive and diffusive-dispersive shock waves for nonconvex conservation laws. *SIAM Review*. 2017;59(1):3-61.
18. Hascoet E, Herrmann HJ. Shocks in non-loaded bead chains with impurities. *Eur Phys J B*. 2000;14:183-190.
19. Herbold EB, Nesterenko VF. Solitary and shock waves in discrete strongly nonlinear double power-law materials. *Appl Phys Lett*. 2007;90(26):261902.
20. Molinari A, Daraio C. Stationary shocks in periodic highly nonlinear granular chains. *Phys Rev E*. 2009;80:056602.
21. Kim H, Kim E, Chong C, Kevrekidis PG, Yang J. Demonstration of dispersive rarefaction shocks in hollow elliptical cylinder chains. *Phys Rev Lett*. 2018;120:194101.
22. Jia S, Wan W, Fleischer JW. Dispersive shock waves in nonlinear arrays. *Phys Rev Lett*. 2007;99:223901.
23. Jian L, Chockalingam S, Cohen T. Observation of ultraslow shock waves in a tunable magnetic lattice. *Phys Rev Lett*. 2021;127:014302.
24. Holian BL. Atomistic computer simulations of shock waves. *Shock Waves*. 1995;5(3):149-157.
25. Tsai DH, Beckett CW. Shock wave propagation in cubic lattices. *J Geophys Res*. 1966;71(10):2601-2608.
26. Duvall GE, Manvi R, Lowell SC. Steady shock profile in a one-dimensional lattice. *J Appl Phys*. 1969;40(9):3771-3775.
27. Gurevich AV, Meshcherkin AP. Expanding self-similar discontinuities and shock waves in dispersive hydrodynamics. *Zh Eksp Teor Fiz*. 1984;87:1277-1292.

28. Holian BL, Straub GK. Molecular dynamics of shock waves in three-dimensional solids: transition from non-steady to steady waves in perfect crystals and implications for the Rankine-Hugoniot conditions. *Phys Rev Lett*. 1979;43(21):1598-1600.
29. Mossman ME, Hoefer MA, Julien K, Kevrekidis PG, Engels P. Dissipative shock waves generated by a quantum-mechanical piston. *Nat Commun*. 2018;9(1):4665.
30. Chong C, Herrmann M, Kevrekidis PG. Dispersive shock waves in lattices: A dimension reduction approach. *Physica D*. 2022;442:133533.
31. Lax PD. On dispersive difference schemes. *Physica D*. 1986;18(1):250-254.
32. Herrmann M. Oscillatory waves in discrete scalar conservation laws. *Math Models Methods Appl Sci*. 2012;22(01):1150002.
33. Fermi E, Pasta J, Ulam S. *Studies of Nonlinear Problems. I*. Technical Report, No. LA-1940. Los Alamos National Laboratory; 1955.
34. Whitham GB. Exact solutions for a discrete system arising in traffic flow. *Proc R Soc A Math Phys*. 1990;428(1874):49-69.
35. Goodman J, Lax PD. On dispersive difference schemes. I. *Commun Pure Appl Math*. 1988;41(5):591-613.
36. Kac M, van Moerbeke P. On an explicitly soluble system of nonlinear differential equations related to certain toda lattices. *Adv Math*. 1975;16(2):160-169.
37. Toda M. *Theory of Nonlinear Lattices*. Springer-Verlag; 1989.
38. Holian BL, Flaschka H, McLaughlin DW. Shock waves in the Toda lattice: Analysis. *Phys Rev A*. 1981;24:2595-2623.
39. Kodama Y. Solutions of the dispersionless Toda equation. *Phys Lett A*. 1990;147(8):477-482.
40. Bloch A, Kodama Y. Dispersive regularization of the Whitham equation for the Toda lattice. *SIAM J Appl Math*. 1992;52(4):909-928.
41. Venakides S, Deift P, Oba R. The Toda shock problem. *Commun Pure Appl Math*. 1991;44(8-9):1171-1242.
42. Biondini G, Chong C, Kevrekidis P. On the Whitham modulation equations for the Toda lattice and the quantitative characterization of its dispersive shocks. *arXiv:2312.10755*. 2023.
43. Benzoni-Gavage S, Noble P, Rodrigues LM. Slow modulations of periodic waves in Hamiltonian PDEs, with application to capillary fluids. *J Nonlinear Sci*. 2014;24(4):711-768.
44. Filip AM, Venakides S. Existence and modulation of traveling waves in particles chains. *Commun Pure Appl Math*. 1999;52(6):693-735.
45. Dreyer W, Herrmann M, Mielke A. Micro-macro transition in the atomic chain via Whitham's modulation equation. *Nonlinearity*. 2005;19(2):471-500.
46. Dreyer W, Herrmann M. Numerical experiments on the modulation theory for the nonlinear atomic chain. *Physica D*. 2008;237(2):255-282.
47. Herrmann M, Rademacher JDM. Riemann solvers and undercompressive shocks of convex FPU chains. *Nonlinearity*. 2010;23:277-304.
48. Dafermos CM. *Hyperbolic Conservation Laws in Continuum Physics* (4th ed.). Springer; 2016.
49. El GA. Resolution of a shock in hyperbolic systems modified by weak dispersion. *Chaos*. 2005;15(3):037103.
50. Sprenger P, Bridges TJ, Shearer M. Traveling wave solutions of the Kawahara equation joining distinct periodic waves. *J Nonlinear Sci*. 2023;33(5):79.
51. Mielke A, Patz C. Uniform asymptotic expansions for the fundamental solution of infinite harmonic chains. *Z Anal Anwend*. 2017;36:437-475.
52. Kamchatnov AM. *Nonlinear Periodic Waves and Their Modulations*. World Scientific; 2000.
53. Gavrilyuk S, Shyue K-M. Singular solutions of the BBM equation: analytical and numerical study. *Nonlinearity*. 2021;35(1):388-410.
54. Sandstede B, Scheel A. Defects in oscillatory media: toward a classification. *SIAM J Appl Dyn Syst*. 2004;3(1):1-68.
55. Hairer E, Nørsett SP, Wanner G. *Solving Ordinary Differential Equations I*. Springer-Verlag; 1993.
56. Herrmann M, Rademacher JDM. Heteroclinic travelling waves in convex FPU-type chains. *SIAM J Math Anal*. 2010;42(4):1483-1504.
57. Gorbushin N, Vainchtein A, Truskinovsky L. Transition fronts and their universality classes. *Phys Rev E*. 2022;106(2):024210.

58. Chong C, Geisler A, Kevrekidis PG, Biondini G. Integrable approximations of dispersive shock waves of the granular chain. *arXiv:2402.08218*; 2024.

How to cite this article: Sprenger P, Chong C, Okyere E, Herrmann M, Kevrekidis PG, Hoefer MA. Hydrodynamics of a discrete conservation law. *Stud Appl Math*. 2024;153:e12767. https://doi.org/10.1111/sapm.12767